

The far-IR spectrum of Sagittarius B2 region:¹ Extended molecular absorption, photodissociation and photoionization

Javier R. Goicoechea²

*Departamento de Astrofísica Molecular e Infrarroja, Instituto de Estructura de la Materia,
CSIC, Serrano 121, 28006 Madrid, Spain*

javier@damir.iem.csic.es

and

Nemesio J. Rodríguez-Fernández³

Observatoire de Paris - LERMA. 61, Av. de l'Observatoire, 75014 Paris, France

and

José Cernicharo²

ABSTRACT

We present large scale $9' \times 27'$ (~ 25 pc \times 70 pc) far-IR observations around Sgr B2 using the *Long-wavelength spectrometer* (LWS) on board the *Infrared Space Observatory* (ISO). The spectra are dominated by the strong continuum emission of dust, the widespread molecular absorption of light hydrides (OH, CH and H₂O) and the fine structure lines of [N II], [N III], [O III], [C II] and [O I]. The widespread dust emission is reproduced by a cold component ($T_d \simeq 13$ –22 K) together with a warm component ($T_d \simeq 24$ –38 K) representing $\lesssim 10$ % of the dust opacity. The fine structure line emission reveals a very extended component of ionized gas. The [O III]52 μ m/88 μ m and [N III]57 μ m/[N II]122 μ m line intensity ratios show that ionized gas has an averaged electron density of ~ 240 cm⁻³. The ionizing radiation can be characterized by a hard but diluted continuum, with effective temperatures of ~ 36000 K and a Lyman continuum photon flux

¹Based on observations with ISO, an ESA project with instruments funded by ESA Member States (especially the PI countries: France, Germany, the Netherlands and the United Kingdom) and with participation of ISAS and NASA.

of $\sim 10^{50.4} \text{ s}^{-1}$. The spatial distribution of the ionizing sources respect to the extended cloud and the clumpyness of the medium determine the large scale effects of the radiation. Photo-Dissociation Regions (PDRs) can be numerous at the interface of the ionized and neutral gas. The analysis of the [C II]158 μm and [O I]63 and 145 μm lines indicates a far-UV radiation field of $G_0 \simeq 10^{3-4}$ and a density of $n_H = 10^{3-4} \text{ cm}^{-3}$ in these PDRs. The widespread OH lines are reproduced by nonlocal radiative transfer models for clouds of moderate volume density ($n_{H_2} \simeq 10^{3-4} \text{ cm}^{-3}$) at $T_k \gtrsim 40\text{--}100 \text{ K}$. PDR models can explain the enhanced column density of species such as H_2O , OH and O^0 . However, they fail to reproduce the observed $\text{NH}_3/\text{NH}_2/\text{NH} \simeq 100/10/1$ abundance ratios. For N-bearing species it seems that shock chemistry has to be invoked. The molecular richness in the outer layers of Sgr B2 is probed by the ISO-LWS Fabry-Perot ($\sim 35 \text{ km s}^{-1}$) detections towards Sgr B2(M), where more that 70 lines from 15 molecular and atomic species are observed at high signal to noise ratio.

Subject headings: Galaxy: center — infrared: ISM: lines and bands — ISM: dust, extinction—HII regions — ISM: individual (Sagittarius B2) — ISM: molecules—line:identification

1. Introduction

The Sagittarius B (Sgr B) complex is located in the inner 400 parsec (pc) of the Galaxy, sometimes referred as the Central Molecular Zone (Morris & Serabyn 1996), at $l \sim 0.6^\circ \pm 0.2^\circ$ galactic longitudes. It contains the well known Sgr B2, B1 and G0.6 – 0.0 radio-sources (see Fig. 1b). Sgr B1 lies to the south of the complex and opposite to Sgr B2, it is dominated by extended radio features (see Mehringer et al. 1992). The G0.6 – 0.0 region is situated between Sgr B2 and B1. The velocity of the ionized gas in G0.6–0.0 is also intermediate between that of Sgr B1 and B2 suggesting that these regions are physically associated. Large scale continuum studies show that Sgr B2 is associated with the brightest emission (Pierce-Price et al. 2000) and the most massive cloud of the Galactic Center region (GC) ($10^7 M_\odot$, Lis & Goldsmith 1990). In the following, we assume that it is situated at $\sim 100 \text{ pc}$ from the dynamical center of the Galaxy for a distance of 8.5 kpc (Kerr & Lynden-Bell 1986).

Figure 1a shows a schematic representation of the main components within Sgr B2. In the central region there are three dust condensations labelled as Sgr B2 north (N), middle (M) and south (S) which are situated in a imaginary North-to-South line of $2' (\sim 5 \text{ pc})$. They contain all the tracers of on-going star formation: ultracompact HII regions created by the UV field of newly born OB stars (cf. Benson & Johnston 1984; Gaume & Claussen 1990), X-

ray sources associated with HII regions, X-ray sources with neither radio nor IR counterpart (Takagi et al. 2002), hot cores (HC) of dense material ($T_k=150\text{--}300$ K; $n_{H_2}\simeq 10^7$ cm $^{-3}$) and embedded proto-stars (cf. Vogel et al. 1987; Lis et al. 1993), molecular maser emission in H₂O, OH, H₂CO, CH₃OH and SiO (cf. Mehringer & Menten 1997 and references therein) and high far-IR luminosity ($\geq 7\cdot 10^6$ L $_{\odot}$; Thronson & Harper 1986). These components are embedded in a moderate density ($n_{H_2}\simeq 10^{5-6}$ cm $^{-3}$) cloud of ~ 10 pc in size (Lis & Goldsmith 1991; Hüttemeister et al. 1993). The temperature in the moderate density cloud decreases with the distance from 80 to 40 K except in a ring structure of warm gas ($T_k=100\text{--}120$ K) with a radius of ~ 4 pc (de Vicente et al. 1997). These internal regions are surrounded by an extended lower density ($n_{H_2}\leq 10^4$ cm $^{-3}$) envelope ($\sim 15'$), hereafter the Sgr B2 envelope, of warm gas ($T_k\geq 100$ K; Hüttemeister et al. 1995).

The origin of the observed rich chemistry in the Sgr B2 envelope and its heating mechanisms are far from settled and several scenarios have been proposed. Low-velocity shocks have been traditionally invoked to explain the enhanced gas phase abundances of molecular species such as SiO or NH₃ and the differences between gas and dust temperatures in the Sgr B2 envelope (Martín-Pintado et al. 1997; Flower et al. 1995). The origin of shocks in Sgr B2 have been associated either with large scale cloud-cloud collisions (Hasegawa et al. 1994) or with small scale wind-blown bubbles produced by evolved massive stars in the envelope itself (Martín-Pintado et al. 1999).

The effect of the radiation in the Sgr B2 envelope has been traditionally ruled out because of differences in the gas and dust temperature, the unusual chemistry, and the absence of thermal radio-continuum and ionized gas outside the HII regions and hot cores within the central condensations. The ISO observations presented here reveal the presence of an extended component of ionized gas detected by its fine structure line emission. The presence of widespread UV and X-ray fields illuminating large portions of Sgr B2 could trigger the formation of PDRs and XDRs in the interface between the ionized gas and the self-shielded neutral layers and could influence in the selective heating of the molecular gas. The complexity of the region possibly allows a combination of different scenarios and excitation mechanisms to coexist within the whole complex.

In this paper we study the large-scale properties of Sgr B2 region and the effect of the far-UV radiation by analyzing its far-IR spectrum (43 to 197 μ m). In Sect. 2, we summarize the ISO observations and the data reduction. The resulting spectra are presented and analyzed in the following sections: dust emission (Sect. 3), fine structure lines (Sect. 4) and molecular lines (Sect. 5). Several techniques have been used in the analysis: gray-body fitting, photoionization models, molecular radiative transfer models and comparisons with PDR models. A general overview and a brief summary is given in Sect. 6.

2. Observations and Data Reduction

The far-IR wavelength range covers the spectral signature of several interesting phenomena which are difficult to observe from ground-based telescopes. These include; the fine structure lines of atoms and ions, the high- J /fundamental rotational lines of heavy/light molecules, the low energy bending modes of carbon clusters and the continuum emission peak for the bulk of star forming regions. Therefore, we proposed to use the LWS spectrometer (Clegg et al. 1996) on board ISO (Kessler et al. 1996) to study the large scale distribution and of the dust, the ionized gas, the neutral gas and the molecular content around the Sgr B2 region.

The present study includes the observations of our open time programs in different positions of the Sgr B complex. In addition we also present some LWS observations retrieved from the public ISO Data Archive² (IDA) observations. The main observations are a $9' \times 27'$ raster map that targets 19 individual positions of the complex (see Fig. 1b). The cross-like LWS/grating map is centered near Sgr B2(M) position at $\alpha = 17^h44^m10.61^s$, $\delta = -28^\circ22'30.0''$ [J1950]. Offsets between consecutive positions are $90''$, excepting North-South points with $|\Delta\delta| \geq 450''$ for which a $180''$ spacing was selected. The central position of our maps, Sgr B2(M), has been widely studied at higher resolution by different LWS/FP observations (see references in Table 5).

2.1. LWS AOT L01 Observations

The cross-like map was carried out during August 1996 and February 1997 (target dedicated time numbers [TDTs] 28702130, 28702131, 46900233 and 46900234) using the Astronomical Observation Template (AOT) L01 with a spectral resolution of $0.29 \mu\text{m}$ for the $43\text{--}93 \mu\text{m}$ range (detectors SW1 to SW5) and $0.6 \mu\text{m}$ for the $80\text{--}197 \mu\text{m}$ range (detectors LW1 to LW5). It uses all 10 LWS detectors with beam sizes (Ω_{LWS}) around $80''$. The typical flux accuracy varies from 10 to 50 % depending on the source geometry, the source flux and the particular detector (Gry et al. 2002). Based in the overlapping regions, the agreement in the flux measured by different detectors is found to be better than 10%. Shifting factors $\leq 10\%$ have been applied in some selected detectors to yield a smoothed and aligned continuum spectrum (Fig. 2). Only detector LW2 showed intensities too high by $\sim 20\%$ relative to the neighboring detectors and had to be scaled by a factor of 0.8. The spectra were oversampled at $1/4$ of a resolution element. The long-wavelength data have been defringed

²see <http://www.iso.vilspa.esa.es/ida>

for the interference pattern systematically seen in the AOT L01 spectra of extended sources or point sources which are offset from the optical axis (Swinyard et al. 1996, Fig. 2b).

Depending on the position in the cross-raster, the far-IR spectrum exhibits several OH, CH and H₂O rotational lines and several fine structure lines. We have clearly detected the [O I]63, 145 μm and [C II]158 μm lines in all positions, except in Sgr B2(M). In addition, lines coming from higher excitation potential³ ions such as [N II]122, [N III]57, [O III]52 and 88 μm lines are also detected. The OH (~ 79 μm), [O I]63, [N III]57 and [O III]88 μm lines lie in the overlapping regions of two different LWS detectors. As fluxes agreed within ~ 15 %, we averaged both determinations. Line fluxes were extracted by fitting gaussians after removing a polynomial baseline for each detector coverage. Emission line fluxes are listed in Table 1.

2.2. LWS AOT L04 Observations

The LWS/FP instrument have been used to investigate the atomic and molecular features in Sgr B2(M) at a higher spectral resolution (~ 35 km s⁻¹). The majority of detected lines (see Fig. 7) have been observed in our AOT L04 ISO proposals. The TDTs are: 32201428, 32701751, 47600907, 47600908, 47600909, 47601001, 47601002, and 46900332. However, an extensive inspection and reduction of about +50 TDTs⁴ from the public IDA have been carried out in order to add some detections and average all available lines (see Polehampton 2002 for the AOT L03 detections). The LWS/FP spectrum of Sgr B2(M) includes the [O I], [C II] and [O III] lines (see Fig. 3a and 3b) also detected at lower resolution in the LWS/gratings. In the case of the [O III]52 and 88 μm lines, its clear LWS/FP identification confirms the doubtful detection made in the gratings and shows the importance of increasing spectral resolution. A declination raster (TDT 32201429) of some molecular lines was also carried out up to $\Delta\delta = \pm 270''$. Fig. 10a shows the raster in the ¹⁶OH 119.442 μm line. The richness of the LWS/FP spectrum of Sgr B2(M) suggests that the far-IR spectra of other observed sources can also be much richer than the observed at the grating resolution.

³Excitation potential of observed ionic species are (in eV): 11.26(C II), 14.53(N II), 29.60(N III), 35.12(O III)

⁴The additional AOT L04 observations analyzed were taken by ISO during orbits: 498, 494, 467, 464, 462, 326, 327, 326, and 322 while the additional AOT L03 observations were taken during orbits: 849, 847, 845, 838, 836, 509, 508, 507, 506, 504 and 476.

2.3. Data Reduction

AOT L04 products have been processed and compared through Off-Line-Processing (OLP) pipeline versions 6.0 to 10.1. There are no major differences except that recent pipelines produce $< 10\%$ less absorption in some lines due to continuum level differences from one OLP to another. For the bulk of the observations, the LWS/FP continuum flux in the wavelength coverage of each individual line deviates by $< 30\%$ and this has been taken as the FP flux calibration error. As recommended by the LWS handbook (Gry et al. 2002), we first checked with the continuum level of the AOT L01 observations, and then, a polynomial baseline was fitted to each spectra and adopted as LWS/FP continuum level.

AOT L01, L03 and L04 data were analyzed using the ISO Spectral Analysis Package (ISAP). Typical routines include: deglitching spikes due to cosmic rays, oversampling and averaging individual scans, defringing the long-wavelength detector AOT L01 scans, removing baseline polynomials and extracting line fluxes by fitting gaussians.

3. Widespread far-IR continuum emission: results

All positions around Sgr B2(M) $[(0'', 0'')]$ present their continuum emission peak between 90 and 100 μm (Fig. 2), indicating that the bulk of observed dust has a relatively cold temperature. The far-IR luminosity in the map is $L_{LWS} \simeq 8.5 \cdot 10^6 L_{\odot}$. The strongest IR positions are Sgr B2(M) and (N) $[\sim(0'', 90'')]$, they contribute with $\sim 28\%$ and $\sim 14\%$ to L_{LWS} , respectively. The rest of the positions show decreasing continuum fluxes with increasing distance to Sgr B2(M). For the same distance to Sgr B2(M), the southern points of the cloud have larger fluxes than the Northern ones, while the dust emission in the East-West direction is more symmetrical.

In order to estimate and better constrain the dust temperature and the associated column density of material, we have modeled the observed continuum spectrum as a sum of two gray bodies. A single gray body crudely fits the observed emission in any position. The total continuum flux in the model is given by:

$$S_{\lambda} = (1 - e^{-\tau_{\lambda}^w}) B_{\lambda}(T_w) \Omega_w + (1 - e^{-\tau_{\lambda}^c}) B_{\lambda}(T_c) \Omega_c \quad (1)$$

where $c/w = i$ stands for cold/warm dust components, $B_{\lambda}(T_i)$ is the Planck function at a temperature T_i , τ_{λ}^i is the continuum opacity and Ω_i is the solid angle subtended by the i dust component. We have expressed τ_{λ} at far-IR wavelengths as a function of the 30 μm opacity using a power-law with exponent β ($\tau_{\lambda} = \tau_{30}(30/\lambda)^{\beta}$). In addition, τ_{30} can be written as a

function of the visual extinction (A_V) as $\tau_{30} = 0.014 A_V$ (Draine 1989). Thus, τ_λ is given by:

$$\tau_\lambda^{c/w} = 0.014 A_V (30/\lambda)^\beta \quad (2)$$

Taking into account the large extension of the dust emission in the region we have considered that both dust components fill the beam for all the observed positions ($\Omega_i = \Omega_{LWS}$). Note that Eq. 1 applies for all positions but not for Sgr B2(M,N) that will be discussed below.

We have tried to fit the continuum emission with β between 1.0 and 2.0, which are the expected emissivity exponents for silicates and graphite grains (Sptizer 1979). We obtain satisfactory fits in this range of β values. However, fits obtained for $\beta \sim 1$ are slightly better (χ^2 two times lower). In addition, the visual extinction derived for $\beta \sim 2$ are more than a factor of 10 larger than the extinction expected from the molecular column densities. Thus, $\beta \gtrsim 2$ seems unrealistic for far-IR wavelengths. β values between 1–1.5 are in agreement with those derived from ISO observations of other GC clouds by Lis & Menten (1998). Note that $\beta \sim 2$ has been obtained from the optically thin emission at 350 and 800 μm around Sgr B2 (Lis & Carlstrom 1994; Dowell et al. 1999). However, the central regions of the cloud ($\lesssim 180''$) are characterized by $\tau_{100} \gtrsim 1$, so that the continuum is optically thick in most of the far-IR wavelengths. Hence, the dust emission observed by ISO basically arises in the external layers of the cloud, i.e., the extended envelope that veils the dense star forming regions, while a considerable fraction of the submillimeter (submm) emission comes from the dense regions of Sgr B2. In addition, the extended dust component observed by ISO is partially filtered out by the beam switching submm observations. Thus, far-IR and submm observations could trace different dust components. In the following, all calculations have been carried out for β values in the range 1.0–1.5.

Table 3 lists the lower and upper limits to the visual extinction. The extinction varies from $A_V \gtrsim 250$ mag for the positions within a radius of $90''$ (~ 4 pc) to $A_V \gtrsim 50$ mag for positions within $270''$ (~ 10 pc).

Table 2 gives the dust temperatures (unlike the visual extinction, T_d is only weakly dependent on β). The spectral energy distributions are best fitted with a dust component with a temperature of 13–22 K and a warmer component with a temperature of 24–38 K. The higher dust temperatures are those measured in the southern regions. The warmer component contributes less than 10 % to the total extinction. For comparison, Gordon et al. (1993) derived $T_d \simeq 19$ K for a smaller region ($95'' \times 270''$) using millimeter observations and graybody analysis, while they obtained IRAS 100 $\mu\text{m}/60 \mu\text{m}$ color temperatures of ~ 35 K. The IRAS observations are more sensitive to the GC diffuse dust (Gordon et al. 1993). The properties of this diffuse component (temperature and opacity) agree with those derived for the warm component in our fits to the far-IR emission of Sgr B2.

3.1. Sgr B2(M) and Sgr B2(N)

One of the main properties of the Sgr B2 central region is the tricky Sgr B2 (N)/(M) continuum flux ratio (N/M) as a function of the observed wavelength. The observational evidence that $N/M < 1$ at $53\ \mu\text{m}$ (Harvey et al. 1977), while $N/M > 1$ at $1300\ \mu\text{m}$ (Goldsmith et al. 1987), can be explained if Sgr B2(N) is embedded behind the dust and gas envelope of Sgr B2(M). Thus, the Sgr B2(N) line of sight will have a larger column density of dust producing a greater emission at millimeter wavelengths. However, at far-IR wavelengths, part of the warm dust emission from Sgr B2(N) will be absorbed by the cooler foreground dust associated to Sgr B2(M), resulting in a $N/M < 1$ ratio (Thronson and Harper 1986; Goldsmith et al. 1990). From the present LWS observations of Sgr B2(M,N), we found $N/M = 0.3$ at $57\ \mu\text{m}$ and $N/M = 0.7$ at $178\ \mu\text{m}$. These ratios confirm the importance of dust opacity even at $\sim 180\ \mu\text{m}$. Due to the large dust opacity in the obscured Sgr B2(M,N) positions, we have only fitted a single graybody to extract the averaged dust temperature and opacity. From the fits we infer $\tau_{100} \simeq 3.8 \pm 0.4$ ($T_d \simeq 31 \pm 1\ \text{K}$) and $\tau_{100} \simeq 5.3 \pm 0.6$ ($T_d \simeq 26 \pm 1\ \text{K}$) for Sgr B2(M) and (N), respectively (see Fig. 2a).

4. Fine structure lines: results

4.1. Extinction corrections

The large H_2 column densities (up to $10^{25}\ \text{cm}^{-2}$) found across Sgr B2 region, suggest that even in the far-IR, fine structure lines can suffer appreciable extinction. In addition, the averaged interstellar extinction toward the GC, with $A_V \simeq 25\ \text{mag}$ (cf. Schultheis et al. 1999), also contributes to the attenuation of atomic emission. In this work we estimate limits to the extinction in each position by using two approximations. A lower limit to the extinction can be obtained using the $[\text{O III}]52$ to $[\text{O III}]88\ \mu\text{m}$ (hereafter $[\text{O III}]52/88$) line intensity ratios. This ratio can not be lower than ~ 0.55 , which is the value obtained in the low electron density limit if lines are optically thin. For those positions where the $[\text{O III}]52/88$ ratios are lower than the lower limit, we derive a minimum visual extinction of $\sim 20\ \text{mag}$ for very distant positions ($\geq 7.5'$) from Sgr B2(M), while a minimum extinction of $\sim 100\ \text{mag}$ inside the $15'$ diameter cloud have been found.

A more direct estimation of the prevailing extinction was obtained from the continuum analysis (Sect. 3). Note that the lower limit to A_V derived from the $[\text{O III}] 52/88$ ratios is consistent with that derived from the dust models (Table 3). In the subsequent discussion we have corrected the line intensities by the extinction limits presented in Table 3.

4.2. The ionized gas

The [O III] lines shown in Fig. 3 (see also Fig. 10 for the [N III] and [N II] lines) reveal an extended component of ionized gas in the southern and eastern regions of Sgr B2. In particular, the [O III]88 μm emission extends $\sim 13.5'$ (~ 35 pc) to the south of Sgr B2(M). The smooth decrease of the [O III]88 μm intensity as a function of the distance to Sgr B2(M) suggest that the major contribution to the observed flux arises in an extended component of ionized gas rather than in compact sources. We also note that the G0.6-0.0 and Sgr B1 radio sources could contribute to the ionization in the southern positions.

To study the properties of the ionized gas we have analyzed the [O III]52/88 and the [N III]57 to [N II]122 μm (hereafter [N III]/[N II]) line intensity ratios. Table 3 lists both ratios for all positions after correcting for extinction.

4.2.1. Electron densities

We have used the [O III]52/88 ratio to estimate the electron density in the observed sources (see Rubin et al. 1994). The [O III]52/88 ratio derived from our observation varies between ~ 3 for the central sources to ~ 0.5 for positions located far from Sgr B2(M). Comparing these [O III] ratios with Fig. 1 of Rubin et al. one finds electron densities ranging from $\sim 10^3 \text{ cm}^{-3}$ to $\sim 50 \text{ cm}^{-3}$ for the sources located close and far from Sgr B2(M), respectively. The average electron density in all observed positions is 240 cm^{-3} .

For Sgr B2(M) itself, the [O III] lines are hardly detected with the LWS in grating mode. Nevertheless, Fig. 3a shows their unambiguous LWS/FP detections towards Sgr B2(M). Both [O III] lines appear centered at $v_{LSR} \simeq 50 \pm 15 \text{ km s}^{-1}$ and, as it could be expected, do not show emission/absorption at more negative velocities produced by the foreground gas in the line of sight. From the LWS/FP [O III] line intensities and correcting the [O III] 52/88 line intensity ratio by the ~ 1000 mag of visual extinction derived for Sgr B2(M), we found an electron density of $\sim 10^{4.3 \pm 1.3} \text{ cm}^{-3}$. As expected, the densest ionized material seen in the far-IR is located in the central star forming regions of Sgr B2.

Mehring et al. (1993), from 20 cm interferometric observations ($26'' \times 15''$ in resolution), detected a $\sim 7'$ (~ 20 pc) halo of diffuse emission around Sgr B. The [O III]88 μm line emission in Fig. 3 spreads beyond the radio recombination lines contours of Mehringer et al.

4.2.2. Radiation temperatures

We have used the [N III] 57 and [N II] 122 μm line intensities and followed the method described in Rubin et al. (1994) for ionization-bounded nebulae to derive the effective temperature of the ionizing radiation (T_{eff}). For each position, we have determined the volume emissivities of both the [N III]57 and [N II]122 μm lines for the electron densities derived from the [O III] 52/88 line intensity ratio. With these emissivities it is possible to derive the actual N^{++} to N^+ abundance ratio. From the analysis of Rubin et al. (see their Fig. 4) and from the [N III]57 and [N II]122 μm line intensities, it is possible to derive T_{eff} . Table 3 gives the derived values at several positions. The largest T_{eff} is obtained towards the central positions (~ 36000 K).

It has been pointed out by Shields & Ferland (1994), that the fine-structure lines ratios observed in the GC can be reproduced with higher T_{eff} and a lower incident flux of ionizing photons (low ionization parameters). This would be the case if the ionizing radiation is diluted, i.e., if the medium is clumpy and inhomogeneous, and/or the ionizing sources are located far from the ionized nebulae. Indeed, this is the situation found in the Radio-Arc region, also in the GC, by Rodríguez-Fernández et al. (2001), where an extended ($40 \text{ pc} \times 40 \text{ pc}$) gas component is ionized by hot (~ 35000 K) diluted radiation arising from the Quintuplet and the Arches clusters. They concluded that the radiation reaches large distances due to the inhomogeneity of the medium. If this applies also to the Sgr B2 envelope, then, the T_{eff} derived above should be considered as lower limits.

In this work it is not possible to perform a detailed study of the geometry of the region due to the limited angular and spectral resolution of the ISO data. Instead, we have performed some simple photo-ionization model calculations using the MPE IDL CLOUDY Environment (MICE), which was developed by H. Spoon at the Max-Planck-Institut für extraterrestische Physik (MPE)⁵ and uses CLOUDY 94 (Ferland 1996). To define the shape of the continuum illuminating the nebulae we have taken the stellar atmospheres modeled by Schaerer & de Koter (1997). First, we have modeled the Sgr B2 cloud as an sphere with the density law as taken from Lis & Goldsmith (1990):

$$7 \times 10^5 \text{ (cm}^{-3}\text{)} \quad 0.3 < R \text{ (pc)} < 1.25 \quad (3)$$

$$7 \times 10^5 \left(\frac{1.25}{R} \right)^2 + 2000 \text{ (cm}^{-3}\text{)} \quad 1.25 < R \text{ (pc)} < 22.5 \quad (4)$$

⁵MICE, SWS and the ISO Spectrometer Data Center at MPE are supported by DLR (DARA) under grants 50QI86108 and 50QI94023.

where R is the radius in pc. We have considered an ionizing source in the center of this sphere emitting a Lyman continuum photon flux, $Q(H)$, of $10^{50.3} \text{ s}^{-1}$ (approximately equal to the total $Q(H)$ in Sgr B2(M,N), see Gaume et al. 1995). To define the shape of the ionizing continuum we have used a 37800 K atmosphere (similar to the maximum T_{eff} derived with the nitrogen lines ratio). The results show that the radius of the [N II] region would not be larger than 1 pc. The same is true for models with $Q(H)=10^{51.3} \text{ s}^{-1}$ and a 41700 K atmosphere. With such a dense and homogeneous model it is not possible to explain the large extension of the ionized gas component observed with ISO. However, if the cloud around the newly born *OB* stars is inhomogeneous and clumpy enough, the UV radiation field can illuminate several surfaces along the line of sight (Tauber & Goldsmith 1990). This scenario was required in the past to explain the first extended [C II] and [C I] observations in molecular clouds (e.g., Phillips & Huggins 1981). Moreover, the poor correlation between the HC₃N and C¹⁸O extended emission found around Sgr B2 suggests that both the envelope and the dense regions are clumpy and/or fragmented (Lis & Goldsmith 1991; Goldsmith et al. 1992).

Instead of doing a complex three-dimensional inhomogeneous density model, we have treated the different observed positions as independent nebulae located at a distance from Sgr B2(M) equal to their projected distance in the plane of the sky. The model assumes that the medium is inhomogeneous and that the radiation arising from Sgr B2(N,M) can reach all the observed positions but, of course, it takes into account the dilution caused by the distance of the different sources to Sgr B2(M). This is done by means of a ionization parameter, U , defined as: $U = Q(H)/4\pi n_e c D^2$, where n_e is the electron density, c is the speed of light and D the distance of the nebula to the ionizing source. We take $n_e=240 \text{ cm}^{-3}$ (the average density derived from the [O III] lines) for all positions.

Figure 4 illustrates the results of some of these models in terms of the [N III]/[N II] ratio versus the distance in arcsec to Sgr B2(M) for the north-south raster. Black lines show that the observed line ratios can be reproduced with $Q(H) \simeq 10^{50.3} \text{ s}^{-1}$ arising from the center of the cloud and T_{eff} between 35500 (dashed lines) and 36300 K (dot-dashed lines). Unfortunately, the large error-bars due to the extinction uncertainties make difficult a more precise analysis. However it seems that the [N III]/[N II] ratios in the southernmost positions are somewhat higher than would be expected from the points closer to Sgr B2(M) and from model calculations. This should be an effect of the presence of additional ionizing sources in the Sgr B1 area. We have tried to model the effect of Sgr B1 assuming that the effective temperature of the radiation arising from these sources is similar to that arising from Sgr B2(M) and to estimate a total ionization parameter defined as:

$$U = \frac{1}{4\pi n_e c} \left(\frac{Q(H)_2}{D_2^2} + \frac{Q(H)_1}{D_1^2} \right) \quad (5)$$

where $Q(H)_2$ and $Q(H)_1$ are the Lyman continuum photons arising from Sgr B2(M) and Sgr B1, respectively, and D_2 and D_1 are the distance of the observed sources to Sgr B2(M) and Sgr B1, respectively. Grey lines in Fig. 4 show the results of some of these combined models with $Q(H)_1 = 10^{49}$ or $10^{49.5} \text{ s}^{-1}$ (Mehring et al. 1992). Including the effect of Sgr B1 helps to explain the observed ratios in the $(0'', -450'')$ and $(0'', -630'')$ positions, but the measured ratio in $(0'', -810'')$ is still higher than expected. Hence, additional ionizing sources in the southern region of Sgr B2 cannot be ruled out.

In any case, it is important to remark that even taking into account the simplicity of the model and the dust extinction uncertainties, the agreement of the model with the observations is fairly good. All measured ratios lie in between the 35500 and the 36300 K curves (see Fig. 4). We conclude that the whole Sgr B complex is permeated by hot radiation arising mainly from Sgr B2(M,N). There is also a contribution to the large scale ionization from sources located in the vicinity of Sgr B1. Minor contribution from additional ionizing sources cannot be ruled out. The long-range effects of the ionizing radiation can only be understood if the medium is clumpy and inhomogeneous, but also if the location and geometry distribution of the ionizing sources is appropriate to ionize predominantly the southern and eastern regions.

4.3. Photodissociation regions

The detection of a widespread component of ionized gas suggests that numerous PDRs can exist in the interface between this ionized material and the molecular gas throughout the cloud. Even more, the prevailing far-UV radiation field and the X-ray emission can also be important in the heating and in the chemistry of the neutral gas. In the following sections we analyze the fine structure emission related with the PDRs and the molecular content of Sgr B2 as seen by far-IR spectroscopy.

4.4. The $[\text{N II}]$ vs. $[\text{C II}]$ correlation

The chemistry and the heating of a PDR are basically controlled by the hydrogen gas density (n_H) and by the far-UV ($6 \text{ eV} < h\nu < 13.6 \text{ eV}$) radiation field. The main coolants in a PDR are the far-IR continuum emission of dust and the $[\text{C II}]$ and $[\text{O I}]$ fine structure lines. Thus, their relative intensities can be used as a diagnostic of the PDR conditions. The first step, hence, is to find the way to distinguish the diffuse ionized gas from the PDR one.

If ionized and neutral/PDR phases exist and/or are associated, [C II] emission can arise from both components (Heiles 1994). For positions with [N II] detections, the [C II] emission coming from the diffuse gas should scale with the [N II] lines because the bulk of N^{++} emission arises in the low-density ionized gas ($\sim 75\%$ according to Malhotra et al. 2001). Figure 5 shows the good correlation found in the Sgr B2 region. The lack of [C II] emission in the grating spectra of Sgr B2(M,N) is a combined effect of extinction, self-absorption in foreground clouds and absorption of the continuum by C^+ in low-excitation diffuse clouds (see the absorption in Fig. 3a). Those observations were not included in the correlation. However, the line is well detected further from the central position where the extinction is less considerable and there is less background continuum to be absorbed by the diffuse component. The resulting observational correlation is:

$$I(C^+)_{-11} \simeq 5.2 \cdot I(N^+)_{-11} + 6.4 \quad (6)$$

where $I(C^+)_{-11}$ and $I(N^+)_{-11}$ are the 158 and 122 μm line intensities in units of $10^{-11} \text{ W cm}^{-2} \text{ sr}^{-1}$. A crude approximation to the [C II] emission arising in PDR gas can be estimated by assuming that the second term in relation 6 represent the averaged [C II] emission in the PDRs. For comparison, Malhotra et al. (2001) derived the theoretical scaling $I(C^+) = 4.3 \cdot I(N^+) + I(C^+)_{PDR}$. However, a linear correction for the diffuse [C II] emission and the same value for all the PDRs in the complex could be a rather crude approximation to the structure and physical conditions of these PDRs.

4.5. PDR diagnostics

Once we have estimated the amount of [C II] arising from PDRs, we can compare the usual far-IR diagnostics: [C II] 158, [O I]63 and 145 μm lines and continuum emission, with theoretical PDR models to estimate the gas density and the far-UV incident field.

Because of the prominent foreground absorption in the [C II] 158 and [O I]63 μm lines observed towards Sgr B2(M), we have omitted⁶ the (M,N) positions in the following discussion (see Vastel et al. 2002). Fig. 6 shows PDR models predictions of the [C II]/[O I] ratio vs. [C II]+[O I]+[Si II]/far-IR ratio in terms of the density, n_H , and the far-UV incident flux, (G_0 ; in units of the local interstellar value) taken from Wolfire, Tielens and Hollenbach (1990, hereafter WTH90). Nevertheless, Simpson et al. (1997) underlined that Si is highly depleted

⁶The LWS/FP spectra of the [O I]63 μm line at $\Delta\delta = \pm 180''$ away from Sgr B2(M) shows the line in emission at Sgr B2 velocities ($\sim 60 \text{ km s}^{-1}$) and no foreground absorption (Lis et al. 2001). Here we consider that outside the bright Sgr B2(M,N) lines of sight, the bulk of observed [O I] emission arises in Sgr B2.

in WTH90 models so that the effect of the not observed [Si II] line across the region can be neglected. Experimental points in Fig. 6 do not include the [Si II]35 μm line because only the central position has been observed (Goicoechea & Cernicharo 2002, hereafter GC02). The uncorrected line intensity ratio in Sgr B2(M) is $[\text{C II}]158/[\text{Si II}]35 \simeq 10$, with the [C II] intensity coming from the emission component (see Fig. 3a for the LWS/FP line).

Squares and triangles in Fig. 6 show the parameter space occupied by Sgr B2. Dark gray triangles represent line ratios that consider all the observed [C II] intensity at each position and light gray squares only consider the mean PDR [C II] emission derived from the correlation with [N II]. The different points show the intensity ratios corrected for the minimum (filled) and maximum (not filled) visual extinction (see Table 3). The data scatter over the $G_0 \simeq 10^{3-4}$ and $n_H \simeq 10^{3-4} \text{ cm}^{-3}$ curves. The expected PDR surface temperature for those values is $\simeq 300 \text{ K}$ (WTH90), and it can reach $\sim 500 \text{ K}$ if heating by photoelectrons ejected from PAHs and very small grains is included in the models (Kaufman et al. 1999).

The possible errors in the PDR parameters are influenced by the A_V uncertainty of each line of sight, the estimation of the PDR [C II] emission and optical depth effects such as the [C II] absorption seen in Fig. 3a. Additional uncertainty is due to the [O I]63 μm line intensity used as a PDR diagnostic in Fig. 6. The line intensity can be larger if cold foreground gas absorbs part of the emission associated with Sgr B2 also outside (M,N) lines of sight. The line could be also weaker (relative to the [O I]145 μm line) if the emission is saturated due to a high optical depth. Finally, the line intensity could also be overestimated if the majority of the emission arises from other inner regions (mainly molecular) of the cloud and not from the PDRs. In such a case, and assuming that the [O I]63 μm line emission is very thick across Sgr B2, it is difficult to estimate the different contributions to the measured line intensity. Therefore, the main properties of the widespread PDRs in Sgr B2 derived from Fig. 6 should be considered to cover the range of densities $n_H = 10^{3-4} \text{ cm}^{-3}$ the far-UV incident flux $G_0 = 10^{3-4}$.

The ionized component shown in Fig. 3 proves the presence of an extended far-UV radiation field. Although the PDR models can explain the fine structure line intensities, we have also considered the role of shocks in the excitation of [O I] and [C II] lines. Such shocks are known to be present in Sgr B2 (Hüttemeister et al. 1995; Martín-Pintado et al. 1997).

The ratio of the integrated line emission ($[\text{O I}]63 + [\text{C II}]158$) to the integrated far-IR emission in PDRs can not be larger than $\sim 10^{-2}$ due to the low efficiency of the photoelectric heating mechanism. On the other hand, this ratio is at least an order of magnitude larger if the lines arise in shocked gas (Hollenbach & McKee 1989). Thus, the observational ratios in Fig. 6 show that the extended [C II] and [O I] emission is dominated by the PDR scenario.

The absolute intensities can also be compared with PDR and shock models in the range $n_H=10^{3-4}$ cm $^{-3}$. The intensity of the [C II]158 μ m line associated with PDRs estimated from the [N II] vs. [C II] correlation is $\sim 6.4 \times 10^{-11}$ W cm $^{-2}$ sr $^{-1}$, which we found to be consistent with the PDR model predictions of Hollenbach et al. (1991) for $G_0 \sim 10^3$. Only *J*-shocks models (Hollenbach & McKee 1989) predict some [C II] emission but it is orders of magnitude weaker than the observed unless high shock velocities ($v_S \sim 100$ km s $^{-1}$) occur. These velocities are not inferred from the line widths derived from large-scale molecular observations at radio wavelengths (see Hüttemeister et al. 1993 for NH $_3$ lines). Also the averaged absolute intensity of the [O I]145 μ m line, $\sim 2.3 \times 10^{-11}$ W cm $^{-2}$ sr $^{-1}$ (Sgr B2(M,N) not included), agrees within a factor ~ 2 with the PDR model predictions. Finally, the low-velocity ($v_S \sim 10$ km s $^{-1}$) *C*-shocks models of Draine et al. (1983) predict weaker [O I]145 μ m line intensities. Comparing these two model predictions with the observed intensity we estimate that the shock contribution to the [O I] emission in Sgr B2 is 10–30 %.

5. The molecular gas

Most pure rotational lines of light molecules appear in the far-IR and submm domains. The search for these species provides a crucial insight on the chemical pathways leading to the observed richness in molecular clouds. Besides, the far-IR absorption measurements allow to trace more extended and lower density gas (i.e., the envelopes) than the one observed in collision-excited emission surveys. The majority of line surveys in Sgr B2 have been concentrated in Sgr B2 (M,N) and in the millimeter domain (Cummins, et al. 1986; Sutton et al. 1991; Nummelin et al. 1998), but less or nothing is known about the possible extended distribution of the light molecular species.

5.1. Sgr B2(M)

The spectral resolution of the grating observations is rather limited (~ 1000 km s $^{-1}$) and produce strong dilution in the search of molecular features in most ISM sources. In order to have an idea of the line density and molecular carriers we have performed a search with the LWS/FP (~ 35 km s $^{-1}$) in Sgr B2(M). Fig. 7 shows the most abundant species that can be detected with ISO in the far-IR and gives insights of which could be detected with the grating in other positions. Tables 4 and 5 list the observed transitions and their corresponding references in the literature. Molecular features include: Several **rotational lines** of light O-bearing molecules such as H $_2$ O, H $_2^{18}$ O, OH, 18 OH, and H $_3$ O $^+$, N-bearing molecules such as NH, NH $_2$ and NH $_3$ and other diatomic species such as CH, HD or HF; Low

energy **bending modes** of non-polar carbon chains such as C_3 or C_4 (only in the grating). The list of detected molecules could still increase as several weak features remain unidentified (see Polehampton 2002). Atomic features include the **fine structure lines** of [O I], [O III] and [C II]. In the next section we analyze the main molecular lines producing widespread absorption in LWS/grating maps at lower resolution: OH, CH and H_2O .

5.2. Widespread OH, H_2O and CH absorption

Although the spectral resolution in the grating is limited, the broad linewidths observed toward the GC ($\gtrsim 30 \text{ km s}^{-1}$), and Fig. 7 provided here, could help in the detection of the most abundant molecular species at large scale. In Sgr B2 we have confidently detected the prominent absorption from the ground-state rotational lines of OH (~ 79 and $\sim 119 \mu\text{m}$), CH ($\sim 149 \mu\text{m}$), H_2O ($\sim 179 \mu\text{m}$) and $H_2^{18}O$ ($\sim 181 \mu\text{m}$; Cernicharo et al. 1997; possibly contaminated by H_3O^+ , see Goicoechea & Cernicharo 2001) in almost all positions (see Figs. 2c and 2d). This implies that light hydrides are present in a region as large as $25 \text{ pc} \times 70 \text{ pc}$. Other molecular features produce less extended absorption/emission and their definitive assignation will require better spectral resolution. This second group of molecular lines include: H_2O (~ 180 , ~ 175 , ~ 108 , and $\sim 101 \mu\text{m}$); NH_3 (~ 170 and $\sim 166 \mu\text{m}$); OH (~ 163 , ~ 84 and $\sim 53 \mu\text{m}$) and C_4 or C_4H ($\sim 58 \mu\text{m}$; Cernicharo, Goicoechea & Benilan 2002). The rest of the absorption features not present in Sgr B2(M) should be considered with caution. Note that no far-IR rotational line of CO was successfully assigned in any position at the signal-to-noise (S/N) ratio of the grating spectra. However, we have detected the CO $J=7-6$ line towards Sgr B2(M) with an emission peak at $\simeq +50 \text{ km s}^{-1}$ (Goicoechea et al. 2003). This and the LWS/FP H_2O lines from the warm molecular gas in front of Sgr B2(M) will be discussed in a forthcoming paper (Cernicharo et al. 2004, in prep.).

Another striking result of the cross-raster map is the presence of an unidentified absorption feature at $\sim 117 \mu\text{m}$ (U117) in all positions near the OH $119 \mu\text{m}$ line (see Fig. 10). This feature has a nearly constant absorption depth of $\simeq 4\%$ independent of the distance to the central position and is present in all individual scans. Prompted by this detection we inspected the public IDA² observations taken with the LWS/FP in this wavelength range. A tentative carrier is presented in Sect. 5.3.

5.2.1. Large scale OH absorption

According to the chemical models, the hydroxyl radical, OH, is an important intermediary in the formation of many molecules present in both the dense $n_{H_2} \sim 10^4 \text{ cm}^{-3}$ (Bergin et al. 1995) and the diffuse $n_{H_2} \sim 10^2 \text{ cm}^{-3}$ gas (Van Dishoeck & Black 1986). The typical OH abundance in dense molecular clouds is $(0.1-1) \cdot 10^{-7}$. Enhanced abundances are predicted in molecular regions under *C*-shock activity (Draine et al. 1983) and in the outer layers of PDRs where H_2O is being photodissociated (Sternberg & Dalgarno 1995). When applied to Sgr B2(M), the *C*-shock models (Flower et al. 1995) can not reproduce the large OH/ H_2O abundance ratio found in the warm envelope, which seems more consistent with the PDR scenario (GC02). The less self-shielded PDR layers will be also a source of [OI] by means of the OH photodissociation. Although in PDRs [OI] can exist deeper in the cloud than OH (Sternberg & Dalgarno 1995), a correlation between the emission/absorption of both species is expected in the outer layers of the cloud and could be used to follow the ionized-PDR-molecular gas relation.

The present cross-like grating maps show the OH $^2\Pi_{3/2} J = 5/2 \leftarrow 3/2$ ground-state line at $\sim 119 \mu\text{m}$ (Fig. 10) and the $^2\Pi_{1/2} \leftarrow ^2\Pi_{3/2} J = 1/2 \leftarrow 3/2$ cross-ladder line at $\sim 79 \mu\text{m}$ (Fig. 9) over the $\sim 25 \text{ pc} \times 70 \text{ pc}$ region. Both lines may be blended with their ^{18}OH and ^{17}OH isotopomers due to the low resolution of the spectra. The individual OH Λ -doubling line components can not be distinguished (only possible at the FP resolution, see the OH lines in Fig. 7). The $\sim 119 \mu\text{m}$ line is detected in absorption in all directions and remains strong through the map. The mean line absorption depth $\simeq 20\%$ is consistent with saturated OH lines. On the other hand, the $\sim 79 \mu\text{m}$ absorption is observed below the northern $\Delta\delta = 630''$ position but its intensity is more sensitive to the position in the map (see Fig. 8 and Fig. 9). In fact, the $\sim 79 \mu\text{m}$ line absorption depth seems to be tracing the dust continuum variations through the region, but not necessary OH abundances, so that OH column densities are correlated with far-IR emission (upper box in Fig. 8). The absorption produced by the OH $^2\Pi_{1/2} \leftarrow ^2\Pi_{3/2} J = 3/2 \leftarrow 3/2$ line at $\sim 53 \mu\text{m}$ is only clearly detected toward Sgr B2(M,N), absorbing $\simeq 3\%$ of the dust continuum emission. The low S/N ratio of the spectra makes the identification rather difficult in other positions.

Finally, an emission line centered at $\sim 163 \mu\text{m}$ have been found in almost all positions (see Fig. 9). The line intensity, 2% of the continuum, appears to be constant across the region. The emission line probably arises from the OH $^2\Pi_{1/2} J = 3/2 \rightarrow 1/2$ line which has been clearly detected in Sgr B2(M) with the FP. Hence, it is plausible that a fluorescence mechanism (absorption of photons in the $\sim 53 \mu\text{m}$ line and emission in the $^2\Pi_{1/2}$ line at $\sim 163 \mu\text{m}$) similar to that found in Sgr B2(M) by GC02, also operates in the whole region favored by the low density of Sgr B2 envelope and by the large far-IR continuum emission.

At the resolution of the grating mode it is difficult to discriminate which components along the line of sight are producing the absorptions [specially in the lines coming from rotational ground–states of light hydrides such as OH, CH or H₂O (see the wide profiles in Figs. 9b and d)]. For these lines, a considerable fraction of the absorption is produced by the low excitation clouds in the line of sight (see Neufeld et al. 2000). The $\Delta\delta = \pm 270''$ FP declination raster of the OH 119.442 μm line (Fig. 10a) reveals that in all observed positions the absorption is dominated by the cold foreground gas at negative velocities which is not associated with Sgr B2. The line almost absorbs completely the continuum emission and covers a broad velocity range, $\Delta v_{FWHM} \simeq 200 \text{ km s}^{-1}$, much larger than the FP resolution. Lines are thus saturated and imply high opacities.

Another FP line declination raster was carried out in the OH $^2\Pi_{3/2} J = 7/2 \leftarrow 5/2$ excited state at 84.597 μm in order to follow up the excitation of the warm OH gas. The line was confidently detected only toward Sgr B2(M,N). This time, both lines are strictly centered at Sgr B2 velocities without appreciable foreground absorption.

The interpretation of the molecular absorption in the Sgr B2 envelope is not obvious and realistic radiative transfer models taking into account both dust and molecular emission are needed. The dust emission play a significant role because photons emitted by dust grains can excite the far–IR rotational transitions of molecules such as OH. In Sgr B2(M,N) the dust grains can also absorb the photons emitted by the molecules. For prominent clouds like Sgr B2, where the far–IR continuum emission and opacity are substantial, these conditions mean that the external envelope can absorb both the dust emission and the molecular line emission from the inner regions of the cloud (if any emission escapes the core).

The present observations have been modeled with the same nonlocal radiative transfer code (see González-Alfonso & Cernicharo 1993) that we used in the analysis of the OH lines towards Sgr B2(M) at higher resolution (GC02). As few OH rotational lines are clearly detected in the grating spectra, we tried to estimate the approximate physical conditions leading to the observed OH extended emission/absorption. The excitation temperature in the cross–ladder and $^2\Pi_{3/2}$ lines have to be lower than the dust temperature (Table 2) in order to see the lines in absorption. In addition, the $\sim 163 \mu\text{m}$ emission can not be very prominent while the $\sim 84 \mu\text{m}$ line must be almost insignificant outside Sgr B2(M,N) positions (at the limited grating resolution). From this information we found that the widespread OH component has a moderate density, $n(\text{H}_2) = 10^{3-4} \text{ cm}^{-3}$, with lower limit temperatures in the range 100 K [Sgr B2(M,N)] to 40 K (extended envelope). For a given temperature, larger densities will give asymmetrical profiles in the Λ –doubling lines and emission lines will be also apparent in the cross-ladder transitions (not observed at the FP resolution, Fig. 7).

These calculations show that the PDR diagnostics and the OH nonlocal models yield similar physical conditions for the outer layers of Sgr B2.

The opacity in the cross-ladder absorption lines is lower than in the intra-ladder transitions and absorption depth differences from one position to other could reflect OH column density variations together with dust emission differences (see upper box in Fig. 8). The observed lines can be fitted with total OH column densities in the line of sight in the range $(5-10) \cdot 10^{15} \text{ cm}^{-2}$ outside the $\sim 15'$ diameter cloud to $(2-5) \cdot 10^{16} \text{ cm}^{-2}$ inside the $\sim 15'$ cloud.

In addition, a correlation between the OH $\sim 79 \mu\text{m}$ absorption and the [O I] $145 \mu\text{m}$ line emission has been found in the region (lower box in Fig. 8). The lower energy level of the [O I] $^3\text{P}_0 - ^3\text{P}_1$ transition is at 230 K and the emission is optically thin in most of the conditions. The LWS/FP observations of the [O I] $145 \mu\text{m}$ line towards Sgr B2(M) (Fig. 3b) show that the line emission appears only at Sgr B2 velocities ($v_{LSR} > 0 \text{ km s}^{-1}$). Therefore, most of the [O I] $145 \mu\text{m}$ line emission arises from the warm outer layers of Sgr B2, where photodissociation is taking place. On the other hand, PDR models suggest that OH is preferentially produced in the external regions of the PDR. The good [O I] $145 \mu\text{m}$ vs. OH $\sim 79 \mu\text{m}$ correlation confirms that a large fraction of the warm [O I] is produced by the photodissociation of OH and/or it arises in the same warm OH layers.

5.2.2. Large scale H_2O and CH absorption

Besides the OH absorption discussed in the previous section, the fundamental lines coming from the rotational ground-states of CH at $\sim 149 \mu\text{m}$ and ortho- H_2O at $\sim 179 \mu\text{m}$ (see also Cernicharo et al. 1997) are also detected in the cross-like spectrum (Fig. 9). Therefore, in addition to the widespread ionized gas and dust emission, the Sgr B2 envelope can be characterized by its extended molecular content.

The H_2O $\sim 179 \mu\text{m}$ map represents further evidence that water vapor is extended in molecular clouds (cf. Cernicharo et al. 1994, 1997; Snell et al. 2000, Neufeld et al. 2003). In addition, the FP observations of the $\sim 179 \mu\text{m}$ line (Cernicharo et al. 1997; lower panel in Fig. 9b) showed that water is present in Sgr B2, but also in the clouds of the line of sight (see also Neufeld et al. 2000 for the $\sim 557 \text{ GHz}$ line). The full H_2O ($\sim 179 \mu\text{m}$) map shows a smooth variation in the north-to-south direction suggesting that the H_2O content and/or the source excitation also change smoothly across the different lines of sight. The H_2O absorption depth is larger in the central positions around Sgr B2(M) and near Sgr B1 (see Fig. 9b).

The last molecular line detected in all observed positions is the CH $^2\Pi_{3/2} \leftarrow ^2\Pi_{1/2}$ $J = 3/2 \leftarrow 1/2$ line at $\sim 149 \mu\text{m}$. The CH $J=1/2$ ground state of the $^2\Pi_{1/2}$ ladder produced by spin-orbit interaction has parity characteristics of a rotational $^2\Pi_{3/2}$ level (Lien 1984). Therefore, the CH $\sim 149 \mu\text{m}$ line is the analogous to the fundamental OH $^2\Pi_{3/2}$ $J = 5/2 \leftarrow 3/2$ intra-ladder line at $\sim 119 \mu\text{m}$. The Λ -doubling lines are only resolved in the FP spectrum (Fig. 9d). Stacey et al. (1987) detected the CH $\sim 149 \mu\text{m}$ lines with KAO only towards Sgr B2(M). ISO observations show that CH is present in the whole region. Furthermore, the line profile obtained with the FP towards Sgr B2(M) is very similar to that observed with KAO (at a resolution of 62 km s^{-1} and a beam of $55''$). The lines have the same broad profiles seen in fundamental lines of H_2O and OH produced by the foreground clouds not associated with Sgr B2. Two distinct absorption peaks at $\simeq 0$ and $\simeq +50 \text{ km s}^{-1}$ are clearly detected.

For each position in the cross-like map, the CH column density in the ground-state has been estimated considering a single unresolved rotational line. The rotational line strength we have used is the sum of each Λ -doubling line strength calculated from the individual hyperfine transitions. The absorption across the extended region is proportional to the total CH column density. We found column densities for the $^2\Pi_{1/2}$ $J=1/2$ ground level between $(0.8 - 1.8) \cdot 10^{15} \text{ cm}^{-2}$ with the larger values centered around Sgr B2(M,N). Using the FP observations (Fig. 9d), we derive a column density of $1.7 \cdot 10^{15} \text{ cm}^{-2}$ for Sgr B2(M), similar to the value obtained by Stacey et al (1987). We have also searched for several CH excited rotational lines at $\sim 180 \mu\text{m}$, but opposite to OH no other lines have detected (see Cernicharo et al. 1999 for undetected FP lines spectra). The lack of absorption from other lines of CH rather than those connecting with the ground level suggest that the molecule is only abundant in the foreground clouds and in the external layers of Sgr B2 where collisional excitation is unimportant. Thus, the above column densities can be a good approximation to the total CH column density. Only higher spectral resolution maps of the CH $\sim 149 \mu\text{m}$ line will allow the accurate division of these column densities into the different foreground clouds. In the case of the Sgr B2(M) line of sight, only $\sim 30\%$ of the total column density arises from Sgr B2 (Stacey et al. 1987). The lack of CH detections in excited rotational states confirms that this species predominantly appears in low-density clouds. Due to the large continuum opacity at $\sim 149 \mu\text{m}$ and $\sim 180 \mu\text{m}$, the CH emission coming from the inner and denser regions does not contribute much to the far-IR observations. Such CH emission is observed at radio wavelengths (Stacey et al. 1987).

5.3. Far-IR detection of NH₂ and NH

In this section we report the far-IR detection of amidogen, NH₂, and imidogen, NH, key radicals toward Sgr B2(M). It is the first time that the ortho-NH₂ species have been observed in the ISM. We also analyze in more detail the first detection of NH in the dense ISM (Cernicharo, Goicoechea & Caux 2000).

NH₂ is a light and floppy molecule thought to be an important reaction intermediate in the production/destruction of N-bearing molecules such as ammonia. NH₂ is an asymmetrical molecule with a ²B₁ ground electronic state characterized by an intricate rotational spectrum. Because of the 2 equivalent H nuclei, ortho and para modifications can be distinguished. The spin-rotation interaction caused by the unpaired electron splits each rotational level into two sublevels which are further split by hyperfine interactions caused by the ¹⁴N nuclear spin. Additional splitting occurs in the ortho- levels due to the resultant proton spin. Although its presence as a photodissociation product of NH₃ in cometary spectra have been known since early 1940's (Swings, McKellar & Minkowski 1943) its interstellar detection had to wait 50 years until the detection of the 1₁₀-1₀₁ lines of para-NH₂ at millimeter wavelengths towards Sgr B2 (van Dishoeck et al. 1993). This is the only detection of the molecule reported in the ISM. Several far-IR spectral features have been recently observed in the laboratory (Gendriesch et al. 2001 and references therein). Here we report the ISM detection of some of them.

Figure 10b (lower box) shows the three spin-rotational components of o-NH₂ 2₂₀-1₁₁ transition at ~117 μm, while only one spin-rotational component of the para-NH₂ 2₂₁-1₁₀ transition at ~126 μm has been detected. No more low excitation NH₂ rotational lines with E_l < 100 K have been found. The lines are centered at Sgr B2 velocities, without absorption at negative velocities from the foreground clouds. The different spin-rotational line strengths were calculated by adding the individual hyperfine structure line strengths that are listed in *Cologne Database for Molecular Spectroscopy* (CDSM) catalog for NH₂ (Müller et al. 2001). However, ortho- and para- species were analyzed as two different molecules and the energy of the para-levels were referred to the lowest para-level that we assign to 0 K energy. The two different spin-rotational partition functions were then computed. The theoretical line strength ratio for the three ortho-NH₂ 2₂₀-1₁₁ spin-rotational lines is 10.0/5.6/1.1 (S_{117.8}/S_{117.4}/S_{117.1}) while the optical depth ratio derived from FP observations is 10.0/7.3/1.7. This suggests that the $J = 5/2 - 3/2$ line (117.792 μm) is moderately thick. With this ratio we can compute the total opacity of the rotational transition and estimate the ortho-NH₂ column density. Assuming a Boltzmann population of the rotational levels and excitation temperatures between 20 and 30 K ($T_{ex} \leq T_d$) we found $N(o-NH_2) = (1.2 \pm 0.3) \cdot 10^{15} \text{ cm}^{-2}$. We have only detected the more intense spin-rotational component

of the para-NH₂ 2₂₁–1₁₀ transition at $\sim 126.8 \mu\text{m}$. The theoretical line strength ratio for the three lines is 10.0/5.5/1.1 ($S_{126.8}/S_{126.4}/S_{126.0}$). Due to the high continuum level measured by the LWS/FP in the TDT 50601112 at $\sim 126 \mu\text{m}$, and the fact that only three scans were available (low S/N ratio), the other two components are expected to be under the detection limit of the AOT L03 observations. No definitive assignation have been done. Assuming the the component at $\sim 126.8 \mu\text{m}$ is optically thin, we derive $N(\text{p-NH}_2) \sim 4 \cdot 10^{14} \text{ cm}^{-2}$. Van Dishoeck et al., derived $N(\text{p-NH}_2) = (1.3 \pm 0.3) \cdot 10^{15} \text{ cm}^{-2}$ from escape probability calculations. Hence, this value has to be considered as an upper limit to the para- column density if both the submm (ground-state) and far-IR (excited) lines arises from the same gas. It is also possible that far-IR NH₂ rotational lines trace a warmer component of lower column density of material. Taking into account both observations, we estimate a total (ortho- + para-) NH₂ column density of $(1.5\text{--}3.0) \cdot 10^{15} \text{ cm}^{-2}$. The upper limit reflects the para-NH₂ column density derived from submm observations, while the lower limit is an estimation of the $N(\text{p-NH}_2)$ based on far-IR observations.

We have finally explored the possibility that the unidentified feature U117 ($\sim 117.1 \mu\text{m}$) observed in all positions of the raster map (see Fig. 10) arises from the three spin-rotational components of the ortho-NH₂ 2₂₀–1₁₁ transition observed at higher resolution towards Sgr B2 (M) (Fig. 10b). In that case, the widespread absorption will correspond to a nearly constant ortho-NH₂ column density of $\sim 2 \cdot 10^{15} \text{ cm}^{-2}$. However, the unresolved NH₂ line in the gratings should be centered at $\sim 117.6 \mu\text{m}$, which prevents from a definitive assignation to NH₂. In addition, we have studied other possible molecular contributors with significant line strength. In particular, the U117 line could also arise from several *b-type* transitions of slightly asymmetrical species such as HNO, HNCO, or HOCO⁺, or it can be the *Q-branch* of a low energy bending mode of a carbon chain. As a example, theoretical calculations predict a 117–125 μm wavelength for the ν_{11} bending mode of C₇, but no laboratory bands have been still attributed (Kurtz & Adamowicz 1991; Martin et al. 1995).

Also related with the formation/destruction of the widely observed NH₃ molecule is the NH radical. The NH ($X^3\Sigma^-$) rotational spectrum is also complicated by the different angular couplings between the rotation, the electronic spin, and the H and ¹⁴N nuclear spin momenta (cf. Klaus, Takano & Winnewisser 1997). Before our far-IR detection in Sgr B2, NH detections had been only reported in the diffuse and translucent clouds (Meyer & Roth 1991). The enhanced NH column densities found in these environments have been used to support that N-chemistry is dominated by grain-surface reactions instead of gas-phase reactions (Wagenblast et al. 1993).

The LWS/FP can only resolve different spin–rotational components of a rotational line. The two detected lines (Fig. 9a) arise from the $N = 2 \leftarrow 1$ rotational transition with the lower energy level at ~ 45 K. These lines peak at Sgr B2 velocities. The $N = 2 \leftarrow 1$ lines arise from Sgr B2(M) and represent the first detection of this species in a dense molecular cloud. Future observations of the $N = 1 \leftarrow 0$ transition from the fundamental ground–state at ~ 1 THz will provide the signature of the NH present in the diffuse molecular clouds of the line of sight and will complement the observations of NH in translucent clouds through its electronic spectrum. We have computed the spin–rotational line strengths from the individual hyperfine structure line strengths listed in the *JPL catalog* for NH (Pickett et al. 1998). A similar analysis of fine structure to that done with NH_2 was carried out to extract the opacity from the NH $2_3-1_2/2_2-1_1$ optical depth ratio. Assuming an excitation temperature of 20–30 K we derive $N(\text{NH}) = (4 \pm 2) \cdot 10^{14} \text{ cm}^{-2}$.

5.3.1. Nitrogen chemistry and shocks

The ISO observations of Sgr B2(M) have given the opportunity of observing simultaneously the NH_3 , NH_2 and NH species. These molecules represent the best signature of the prevailing N–chemistry in the outer regions of the cloud. Far–IR NH_3 lines have been analyzed by Ceccarelli et al. (2002). Their LVG calculations showed the NH_3 column density in the warm absorbing layers is $(3.0 \pm 1.0) \cdot 10^{16} \text{ cm}^{-2}$. Assuming that NH_3 far–IR and radio (Hüttemeister et al. 1995) lines arise in the same region, they derived large temperatures ($T_k \sim 700$ K), similar to those obtained from radio observations. However, the ammonia observed in absorption against the radio continuum is dominated by the molecular gas in front of the HII regions. Due to the large opacity in the far–IR, the bulk of the gas sampled by ISO only refers to the Sgr B2 envelope embedding the star formation regions.

There is strong evidence that both the NH_3 heating and the observed metastable column densities can be reproduced if grain–surface formation and sputtering by low–velocity shocks are taken into account (Flower et al. 1995). In fact, the same shock models satisfactory explain the recent NH_3 (Ceccarelli et al.) and NH_2 (this work) column densities derived from ISO observations.

The special formation conditions of gas phase NH_3 (grain chemistry and mantle erosion) and its survival conditions (easily photodissociated) suggests that studies of the neutral gas in Sgr B2 by means of the NH_3 absorption are only sensitive to its specific conditions.

We found that the observational $\text{NH}_3/\text{NH}_2/\text{NH}\simeq 100/10/1$ column density ratio can not be explained in terms of dark cloud models, these predict $\text{NH}_3/\text{NH}_2 < 3$ (Millar et al. 1991) and this ratio would be even smaller if photodissociation of NH_3 is included. In addition, Sternberg & Dalgarno (1995) derived a NH_3/NH column density ratio $> 2 \cdot 10^3$ in the region where the incident far-UV field is completely attenuated. A PDR contribution to the observed N-bearing radicals may be possible as photodissociation products of NH_3 . However, current models predict $\text{NH}_2/\text{NH} < 1$ and $\text{NH}_3/\text{NH} < 1$ column density ratios in the regions affected by the far-UV radiation field ($A_V < 5$ mag; Sternberg & Dalgarno 1995), which are not observed at least in the averaged picture given by the large ISO/LWS beam. The large column densities of warm ammonia found in the Sgr B2 envelope (Ceccarelli et al. 2002) can still be compatible with its photodissociation if a notable enhancement in the NH_3 grain-surface formation and an efficient mantle erosion mechanism dominates the ammonia chemistry. Such mechanism are the widespread low-velocity shocks that liberate large amounts of NH_3 from the grains and also heat the NH_3 in the gas phase.

The chemistry in Sgr B2 is a challenging issue as the same shock models that apparently reproduce the N-chemistry (Flower et al. 1995) fail in reproducing the O-chemistry traced by far-IR observations. The predicted H_2O column density is almost two orders of magnitude larger than the observed by ISO (Goicoechea & Cernicharo 2001; Cernicharo et al. 2004, in prep.) while the predicted OH column density is an order of magnitude lower than the observed (GC02). Thus, the large OH abundance seems more related with the photodissociation of H_2O . Recent analysis of the extended $\text{H}_2\text{O } 1_{10} - 1_{01}$ absorption observed by SWAS around Sgr B2 (Neufeld et al. 2003) and of the HDO absorption toward Sgr B2(M,N) (Comito et al. 2003) support the above (ISO) column densities for the water vapor. Finally, the OH absorption is correlated with the warm [O I] emission and this could be related with the OH photodissociation in the outer layers.

6. Summary

The present far-IR continuum and spectral observations of the Sgr B2 region have revealed a new perspective of the less known extended envelope of the complex. The ISO observations show the presence of an extended component of ionized gas reaching very large distances from the regions of known massive star formation. Photoionization models show that high effective temperatures are possible if the ionization parameter is low. We found that the radiation can be characterized by a hard ionizing continuum typical of an O7 star ($T_{eff} \simeq 36000$ K) and the ionization of the Sgr B complex is dominated by Sgr B2.

We suggest that the whole region must be highly clumped and/or fragmented, so that the diffusion of the far-UV radiation field allows the ionized /neutral (warm) /neutral (cold and dense) material to exist throughout the cloud. However, the exact three dimensional location of the ionization sources relative to the extended cloud is not clear, but it also determines the regions preferably illuminated by the UV radiation (southern and eastern regions). It is plausible that the moderate density cloud around Sgr B2(M,N) blocks the ionization radiation in the northern and western directions. Another possibility is the presence of evolved stars and/or young massive stars in the envelope of Sgr B2 itself, so that the UV field on the extended cloud is the averaged interstellar field. The observed X-ray emission could also play a role in the large scale ionization, but the effects on the neutral gas are more difficult to determine. In any case, we have presented observational evidence that gas is photochemically active far from the ionizing sources. This is reflected in the neutral gas heating and in the column densities of some molecules.

In addition, molecular tracers and atomic fine structure tracers do not show evidence of high-velocity shocks. Hence, the ionized gas can not be explained in terms of high-velocity dissociative shocks. It seems that the well established widespread low-velocity shocks (Hüttemeister et al. 1995; Martín-Pintado et al. 1997) are not the only mechanism heating the gas to temperatures larger than those of the dust. Coexistence of mechanical and radiative-type heating mechanisms based on the effects of a UV radiation field that permeates an inhomogeneous medium seems to be the rule in Sgr B2 and also in the bulk of GC molecular clouds observed by ISO (Rodríguez-Fernández et al. 2004, in prep.).

According to the extended distribution of molecular species such as H_2O , OH and CH, and the large column density of key molecular species detected in the Sgr B2(M) position, Sgr B2 is one of the richest and peculiar clouds in the galaxy.

The geometrical properties of Sgr B2 (clumped structure, extended envelope, centrally condensed hot cores and compact HII regions); its physical conditions (high average densities, widespread warm gas, cool dust, turbulence and enhanced interstellar radiation field); and its chemical complexity (some molecules detected only toward Sgr B2 and nowhere else in the Galaxy, extended emission of refractory molecules, etc.) mimics a miniature Galactic Center with only $\sim 15'$ extend. Therefore, Sgr B2 provides a good *template* to study the mean physical and chemical processes in a galactic nucleus with enough spatial resolution, from the developing clusters of hot stars, to the regions without significant luminous internal heating sources, but exposed to the mean GC environment conditions.

The actual far-IR spectral and spatial resolution makes a similar analysis of other galactic nuclei rather speculative. However, it seems tempting that extrapolating the far-IR spectrum of $\approx 10^5$ Sgr B2 clouds to a distance of a few Mpc will yield a similar spectrum to

those existing of normal and IR galaxies such as Arp 220. Recent application of PDR models to different samples of galaxies observed in the far-IR show that the physical conditions of extragalactic PDRs do not differ much from the values derived for Sgr B2 (WHT90; Malhotra et al. 2001). Hence, Sgr B2 also plays a template role for extragalactic ISM studies.

To summarize, we have carried out a medium resolution ($\sim 1000 \text{ km s}^{-1}$) mapping from 43 to $197 \mu\text{m}$ of the Sgr B2 region ($9' \times 27'$) and have observed the Sgr B2(M) central source at high resolution ($\sim 35 \text{ km s}^{-1}$). The main conclusions of this work are:

- The far-IR spectra show an extended region of strong dust emission ($L_{FIR} \simeq 10^7 L_{\odot}$). The observed continuum emission is best fitted with a dust component with a temperature of 13–22 K and a warmer component with a temperature of 24–38 K. The warmer component contributes in less than 10% to the total optical depth.
- The [O III], [N III] and [N II] fine structure line emission has revealed an extended component of ionized gas. The averaged electronic density is $\sim 240 \text{ cm}^{-3}$. The ionizing radiation can be characterized by $T_{eff} \simeq 36000 \text{ K}$ but a low ionization parameter. The total number of Lyman photons needed to explain such component is approximately equal to that of the HII regions within Sgr B2. The southern regions of the Sgr B complex may be also influenced by additional ionizing sources near the location of Sgr B1.
- The location and geometry distribution of the ionizing sources relative to the extended cloud favors the ionization of the southern and eastern regions of Sgr B2. Also the clumpy structure of gas in Sgr B2 that surrounds the ionizing sources allows the radiation to penetrate large distances throughout the envelope, so that PDRs are numerous throughout the cloud at the interface of the ionized and the neutral gas.
- Comparison of the [OI] and [C II] lines with PDR models indicates a $G_0 \simeq 10^{3-4}$ enhancement of the far-UV field and a n_H density of 10^{3-4} cm^{-3} in these PDRs.
- Extended photoionization and photodissociation are also taking place in Sgr B2 envelope in addition to other processes such as widespread low-velocity shocks. The origin of the rich chemistry is probably a result of the combination of both scenarios.
- The ground-state rotational transitions of light hydrides such as OH, CH and H_2O produce absorption in all observed positions representing evidences that these far-IR lines are widespread in molecular clouds.
- Radiative transfer models of OH show that the neutral gas in the external molecular layers have physical conditions ($n_{\text{H}_2} = 10^{3-4} \text{ cm}^{-3}$; $T_k \gtrsim 40\text{--}100 \text{ K}$) in between those derived from the ionized gas and those of the denser gas in the star forming cores.

- The LWS/FP spectrum of Sgr B2(M) shows the most abundant species that could be detected with ISO in the far-IR. The $\text{H}_2\text{O}/\text{OH}/\text{O}^0$ chemistry in the envelope seems dominated by photodissociation processes while the $\text{NH}_3/\text{NH}_2/\text{NH}\simeq 100/10/1$ column density ratios are still better explained under low-velocity shocks activity.

Future far-IR heterodyne instruments, such as HIFI on board the *Herschel Space Observatory* will observe the Sgr B2 region and other galactic nuclei with larger spatial and spectral resolution than ISO. A direct observation of the inhomogeneous nature of the ionized gas, the warm PDRs and the shocked regions will then be possible.

We thank Spanish DGES and PNIE for funding support under grant ESP98-1351-E, PANAYA2000-1785, AYA2000-1888-E, AYA2000-1974-E, and ESP2001-4516 We thank J. Martín-Pintado for stimulating discussions about Sgr B2, M.A. Gordon for providing us the IRAS maps of Sgr B2 and J. Fisher and E. González-Alfonso for useful suggestions. We also thank M.A. Orlandi for help in the data analysis and the anonymous referee for his/her useful comments which resulted in an improvement of the paper. NJR-F has been supported by a Marie Curie Fellowship of the European Community program “Improving Human Research Potential and the Socio-economic Knowledge base” under contract number HPMF-CT-2002-01677.

REFERENCES

- Benson, J.M., & Johnston, K.J. 1984, 277, 181
- Bergin, E.A., Langer, W.D., & Goldsmith, P.F. 1995 ApJ, 441, 222
- Ceccarelli, C. et al. 2002, A&A, 383, 603
- Cernicharo J., González-Alfonso, E., Alcolea, J., Bachiller, R., & John, D. 1994, ApJ, 432, L59
- Cernicharo, J., Lim, T., Cox, P., et al. 1997, A&A, 323, L25
- Cernicharo, J., Orlandi, M.A., González-Alfonso, E., & Leeks, S.J. 1999, in “The Universe as seen by ISO”, Eds. P. Cox & M.F. Kessler, ESA-SP 427, 655
- Cernicharo, J., Goicoechea, J.R., & Caux, E. 2000, ApJ, 534, L199
- Cernicharo, J., Goicoechea, J.R. & Benilan, Y. 2002, ApJ, 580, L157

- Clegg, P.E., et al. 1996, *A&A*, 315, L38
- Comito, C., Schilke, P., Gerin, M., Phillips, T. G., Zmuidzinas, J., Lis, D. C. 2003, *A&A*, 402, 635
- Cummins, S. E., Thaddeus, P., & Linke, R. A. 1986, *ApJS*, 60, 819
- de Vicente, P., Martín-Pintado, J., & Wilson, T. L. 1997, *A&A*, 320, 957
- Dowell, C.D., Lis, D.C., Serabyn, E., et al. 1999, *ASP conf. series*, Vol 186, 457
- Draine, B.T., Roberge, W.G., & Dalgarno, A. 1983, *ApJ*, 264, 485
- Draine, B.T. 1989, in “Infrared Spectroscopy in Astronomy”, ed. Kaldeich B.H., *ESA SP–290*, 93
- Ferland, G.J. 1996, Hazy, A Brief Introduction to Cloudy, University of Kentucky Dept. of Physics and Astronomy Internal Report
- Flower, D.R., Pineau des Forêts, G. & Walmsley, M.C. 1995, *A&A*, 294, 815
- Gaume, R.A., Claussen, M.J., De Pree, C.G., et al. 1995, *ApJ*, 449, 663
- Gendriesch, R., Lewen, F., Winnewisser, G., & Müller, H.S.P. 2001, *J.Mol.Struct.*, 599, 293
- Giesen, T. F., Van Orden, A. O., Cruzan, J. D., et al. 2001, *ApJ*, 551, L181
- Goicoechea, J.R., & Cernicharo, J. 2001, *ApJ*, 554, L213
- Goicoechea, J.R., & Cernicharo, J. 2002, *ApJ*, 576, L77 (GC02)
- Goicoechea, J.R., Cernicharo, J., Pardo, J.R. 2002, Exploiting the ISO Data Archive. Infrared Astronomy in the Internet Age, to be held in Sigüenza, Spain 24-27 June, 2002. Edited by C. Gry et al. To be published as *ESA Publications Series*, *ESA SP-511*.
- Goldsmith, P.F., Snell, R.L., & Lis, D.C. 1987, *ApJ*, 313, L5
- Goldsmith, P.F., Lis, D., et al. 1990, *ApJ*, 350, 186
- Gordon, M. A., Berkemann, U., Mezger, P. G., et al. 1993, *A&A*, 280, 208
- Gry, C., Swinyard, B., Harwood, A., et al. 2002, *The ISO Handbook*, Volume III: LWS - The Long Wavelength Spectrometer.
- Harvey, P. M., Campbell, M. F., & Hoffmann, W. F. 1977, *ApJ*, 211, 786

- Hasegawa, T., Sato, F., Whiteoak, J.B., & Miyawaki R. 1994, *ApJ*, 429, L77
- Heiles, C. 1994, *ApJ*, 436, 720
- Hollenbach, D. & McKee, C.F. 1989, *ApJ*, 342, 306
- Hollenbach, D., Takahashi, T., & Tielens, A.G.G.M. 1991, *ApJ*, 377, 192
- Hüttemeister, S., Wilson, T.L., Henkel, C., & Mauersberger, R. 1993, *A&A*, 276, 445
- Hüttemeister, S., Wilson, T. L., Mauersberger, R., Lemme, C., Dahmen, G., & Henkel, C. 1995, *A&A*, 294, 667
- Kaufman, M.J., Wolfire, M.G., Hollenbach, D.J., & Luhman, M.L. 1999, *ApJ*, 527, 795
- Kerr, F. J., & Lynden-Bell, D. 1986, *MNRAS*, 221, 1023
- Kessler, M.F., et al. 1996, *A&A*, 315, L27
- Klaus, T., Takano, S., & Winnewisser, G. 1997, *A&A*, 322, L1
- Kurtz, J., & Adamowicz, L. 1991, *ApJ*, 370, 784
- Lien, D. J. 1984, *ApJ*, 284, 578
- Lis, D.C., & Goldsmith, P.F. 1990, *ApJ*, 356, 195
- Lis, D.C., & Goldsmith, P.F. 1991, *ApJ*, 369, 157
- Lis, D.C., Goldsmith, P.F., Carlstrom, J.E. & Scoville, N.Z. 1993, *ApJ*, 402, 238
- Lis, D.C., & Carlstrom, J.E. 1994, *ApJ*, 424, 189
- Lis, D.C., Keene, J., Phillips, T. G., Schilke, P., Werner, M.W., & Zmuidzinas, J. 2001, *ApJ*, 561, 823
- Lugten, J. B., Stacey, G. J., & Genzel, R. 1986, *Bulletin of the American Astronomical Society*, Vol. 18, p.1007
- Malhotra, S., Kaufman, M. J., Hollenbach, D., et al. 2001, *ApJ*, 561, 766
- Martin, J.M.L., El-Yazal, J., & François, J.P. 1995, *Chem.Phys.Lett.* 242, 570
- Martín-Pintado, J., de Vicente, P., & Fuente, A., & Planesas, P. 1997, *ApJ*, 482, L45

- Martín-Pintado, J., Gaume, R. A., Rodríguez-Fernandez, N. J., de Vicente, P., & Wilson, T. L. 1999, *ApJ*, 519, 667
- Mehring, D. M., Yusef-Zadeh, F., Palmer, P., & Goss, W. M. 1992, *ApJ*, 401, 168
- Mehring, D. M., Palmer, P., Goss, W. M., & Yusef-Zadeh, F. 1993, *ApJ*, 412, 684
- Mehring, D. M., Menten, K.M. 1997, *ApJ*, 474, 346
- Meyer, D.M., & Roth, K.C. 1991, *ApJ*, 376, L49
- Millar, T. J., Bennett, A., Rawlings, J. M. C., Brown, P. D., & Charnley, S. B. 1991, *A&AS*, 87, 585
- Morris, M., & Serabyn, E. 1996, *ARA&A*, 34, 645
- Müller, H.S.P., Thorwirth, S., Roth, D. A., & Winnewisser, G. 2001, *A&A*, 370, L49
- Neufeld, D.A., Zmuidzinas, J., Schilke, P., & Phillips, T.G. 1997, *ApJ*, 488, L141
- Neufeld, D.A., Ashby, M.L.N., Bergin, E.A., et al. 2000, *ApJ*, 539, L111
- Neufeld, D.A., Bergin, E.A., Melnick, G.J., & Goldsmith, P.F. 2003, *ApJ*, 590, 882
- Nummelin, A., Bergman, P., Hjalmarson, A., Friberg, P., Irvine, W.M., Millar, T. J., Ohishi, M., & Saito, S. 1998, *ApJS*, 117, 427
- Phillips, T. G., & Huggins, P.J. 1981, *ApJ*, 251, 533
- Picket, H.M., Polnyter, R.L., Cohen, E.A., Delitsky, J.C. & Müller, H.S.P. 1998, *J. Quant. Spectrosc. Radiat. Transfer*, 60, 883
- Pierce-Price, D., Richer, J.S., Greaves, J.S. et al. 2000, *ApJ*, 545, L121
- Polehampton, E. T. 2002, Ph.D. thesis, Linacre College, Oxford, UK.
- Polehampton, E. T., Baluteau, J.-P., Ceccarelli, C., Swinyard, B. M., Caux, E. 2002, *A&A*, 388, L44
- Rodríguez-Fernandez, N. J., Martín-Pintado, J., & de Vicente, P. 2001, *A&A*, 377, 631
- Rubin, R.H., Simpson, J.P., Lord, S.D., et al. 1994, *ApJ*, 420, 772
- Thronson, H.A., & Harper, D.A. 1986, *ApJ*, 300, 396
- Schaerer, D., & de Koter, A. 1997, *A&A*, 322, 598

- Schultheis, M., Ganesh, S., Simon, G., et al. 1999, *A&A*, 349, L69
- Shields, J. C. & Ferland, G. J. 1994, *ApJ*, 430, 236
- Simpson, J.P., Colgan, S.W.J., Cotera, A.S., Erickson, E.F., Haas, M.R., Morris, M., & Rubin, R.H. 1997, *ApJ*, 487, 689
- Snell, R.L., Howe, J.E., Ashby, M.L.N., et al. 2000, *ApJ*, 539, L93
- Spitzer, L. 1978, *Physical Processes in the Interstellar Medium*, New York: Wiley
- Stacey, G.J., Lugten, J. B., & Genzel, R. 1987, *ApJ*, 313, 859
- Sternberg, A., & Dalgarno, A. 1995, *ApJS*, 99, 565
- Storey, J., Watson, D.M., & Townes, C.H. 1981, *ApJ*, 244, L27
- Sutton, E. C., Jaminet, P. A., Danchi, W. C., Blake, & G.A. 1991, *ApJS*, 77, 255
- Swings, P., McKellar, A., & Minkowski, R. 1943, *ApJ*, 98, 142
- Swinyard, B. M., Clegg, P. E., Ade, P. A. R., et al. 1996, *A&A*, 315, L43
- Takagi, S., Murakami, H., Koyama, K. 2002, *ApJ*, 573, 275
- Tauber, J.A., & Goldsmith, P.F. 1990, *ApJ*, 356, L63
- van Dishoeck, E.F., & Black, J.H. 1986, *ApJS*, 62, 109
- van Dishoeck, E.F., Jansen, D.J., Schilke, P., & Phillips, T. G. 1993, *ApJ*, 416, L83
- Vastel, C., Polehampton, E. T., Baluteau, J.-P., Swinyard, B. M., & Caux, E., Cox, P. 2002, *ApJ*, 581, 315
- Vogel, S.N., Genzel, R., & Palmer, P. 1987, *ApJ*, 316, 243
- Wagenblast, R., Williams, D. A., Millar, T. J., & Nejad, L. A. M. 1993, *MNRAS*, 260, 420
- Wolfire, M.G., Tielens, A. G. G. M., & Hollenbach, D. 1990, *ApJ*, 358, 116 (WTH90)

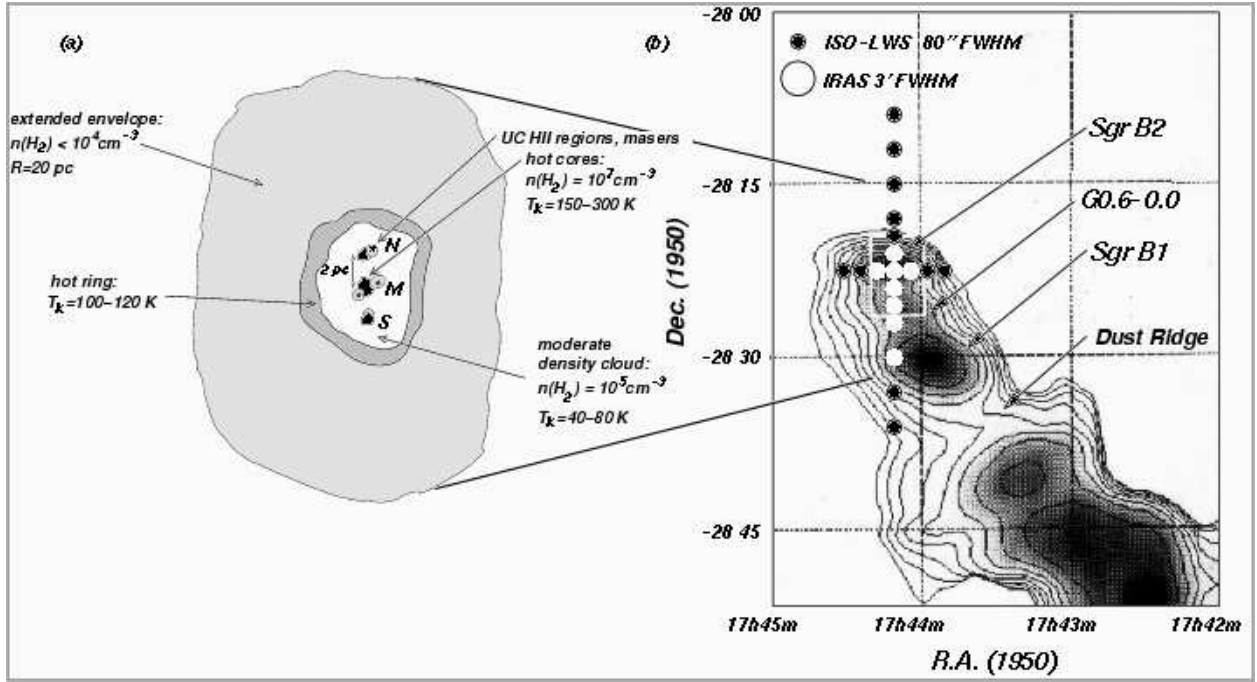


Fig. 1.— (a): Sketch showing the different structures and components in the Sgr B2 region. Hot cores are shown black shaded and HII regions are the structures enclosing the stars (adapted from Hüttemeister et al. 1995). (b): Large scale IRAS image at $60 \mu\text{m}$ (Gordon et al. 1993) and ISO-LWS target positions across Sgr B2 region.

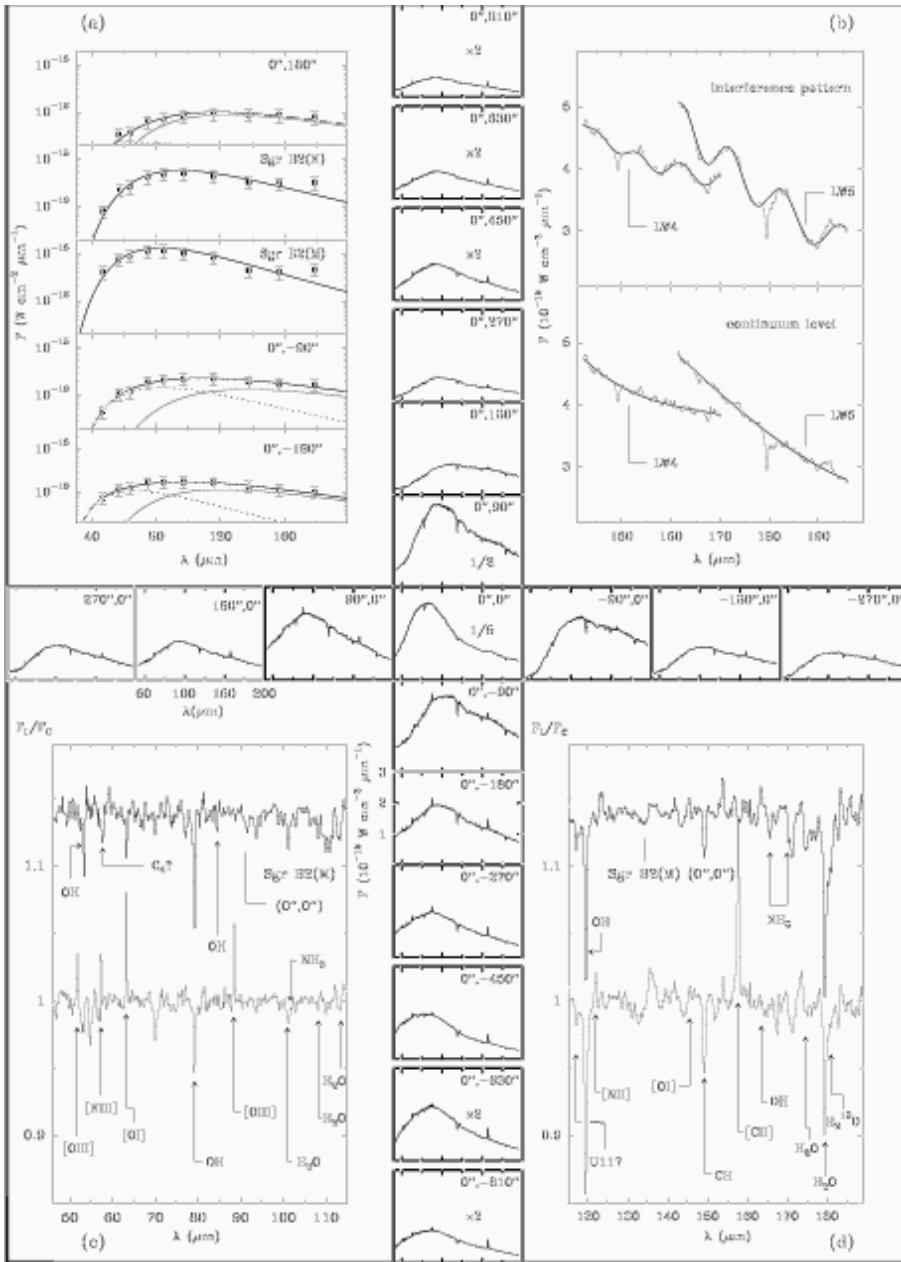


Fig. 2.— Raster map obtained with the LWS grating between 43–197 μm with a spectral resolution of $\sim 1000 \text{ km s}^{-1}$. In each box, offset positions are given in arcsec respect to the $(0'', 0'')$ central position at: $\alpha = 17^{\text{h}}44^{\text{m}}10.61^{\text{s}}$, $\delta = -28^{\circ}22'30.0''$ [J1950]. The intensity scale corresponds to the flux (in units of $10^{-16} \text{ W cm}^{-2} \mu\text{m}^{-1}$) and the abscissa to the wavelength in μm . (a) Averaged continuum flux of each LWS detector and gray-body best fits (black) for some selected positions. Dotted line corresponds to the warm component and continuous grey line to the cold component. The error bars correspond to a 30% of flux uncertainty. (b) *Top*: Observed fringing in the long-wavelength detectors. *Bottom*: Continuum level after defringing the spectra. (c) and (d) Comparison of LWS grating spectra of Sgr B2(M) $(0'', 0'')$ [black] and an average of $(90'', 0'') + (0'', -90'') + (0'', -180'')$ adjacent positions [grey]. A polynomial baseline have been removed.

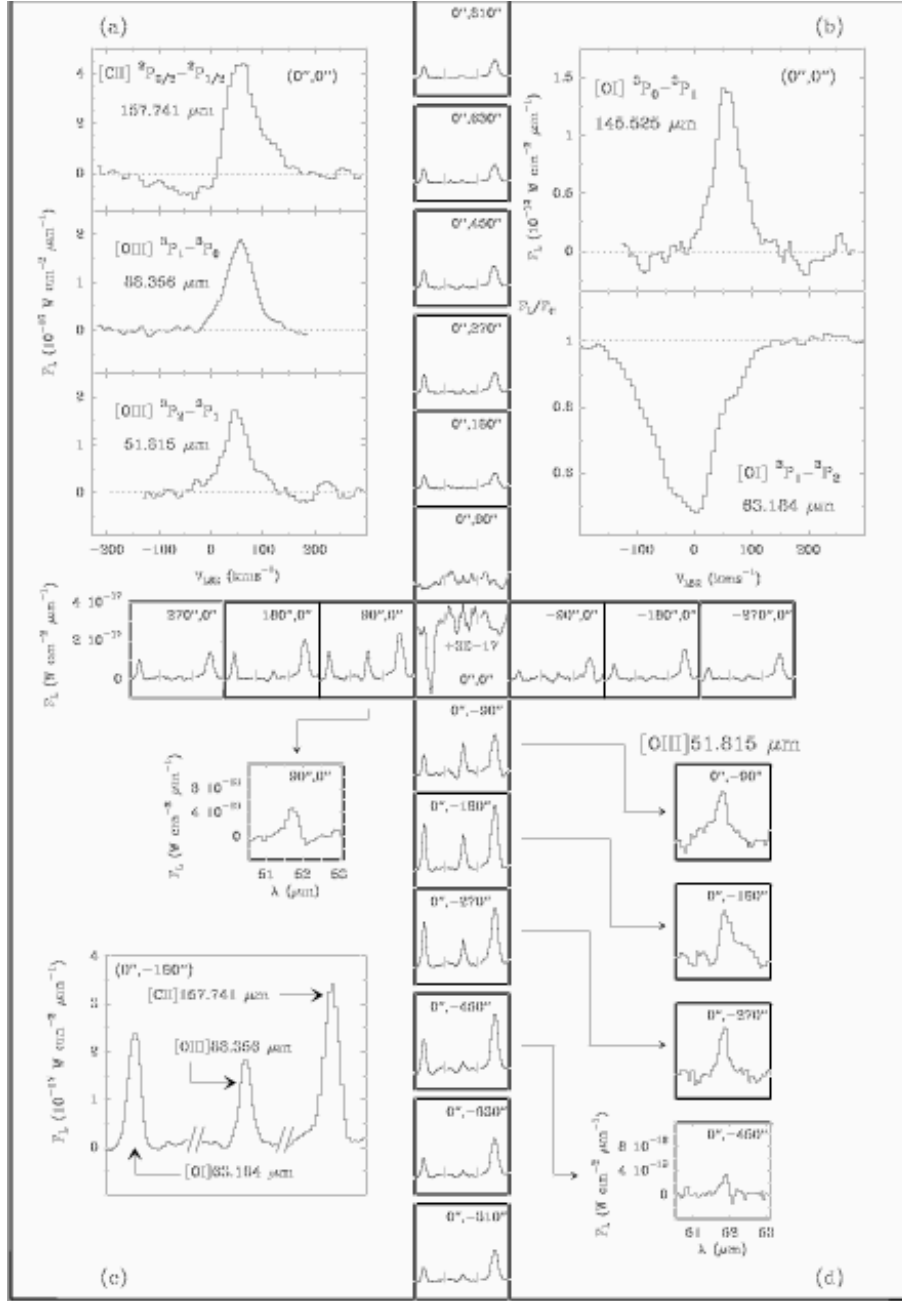


Fig. 3.— Raster map obtained with the LWS grating of the [O I]63, [O III]88 and [C II]158 μm lines. In each box, offset positions are given in arcsec respect to the $(0'', 0'')$ central position at: $\alpha = 17^h 44^m 10.61^s$, $\delta = -28^\circ 22' 30.0''$ [J1950]. The intensity scale corresponds to line flux and the abscissa to the wavelength. (a) [C II] and [O III] lines detected with LWS-FP in $(0'', 0'')$ (b) [O I] lines detected with LWS-FP in $(0'', 0'')$. (c) Main features of the grating raster map labelled. (d) Raster map positions with clearest [O III]52 μm detections.

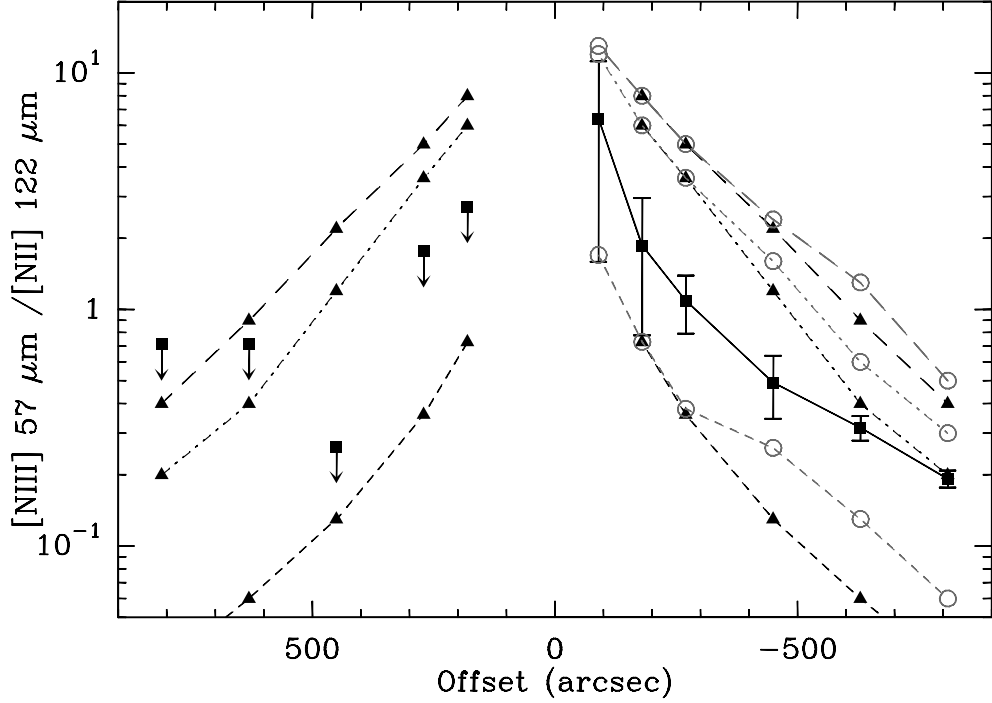


Fig. 4.— Solid squares show the $[N III]57 \mu m / [N II]122 \mu m$ lines ratios derived from the observations for the north-south raster. The arrows indicate that those points are upper limits. The error-bars are due to the uncertainties in the extinction correction. Upper limits for Sgr B2(M) $[(0'',0'')]$ and Sgr B2(N) $[(0'',90'')]$ are not significant and therefore they are not shown. The solid triangles and empty circles show the photo-ionization models results for $n_e=240 \text{ cm}^{-3}$ taking into account Sgr B2 (triangles) and both Sgr B2 and Sgr B1 (circles). Points from a same model are connected by lines. The black dashed line and the triangles show the model results for $T_{eff}=35500 \text{ K}$ and $Q(H)_2=10^{50.3} \text{ s}^{-1}$. The grey dashed line and circles represents the results considering additional $Q(H)_1=10^{49.5} \text{ s}^{-1}$ from Sgr B1. The dot-dashed lines and the triangles represents the results for $T_{eff}=36300 \text{ K}$ and $Q(H)_2=10^{50.3} \text{ s}^{-1}$. The grey line with circles has additional $Q(H)_1=10^{49.0} \text{ s}^{-1}$. The long-dashed lines with triangles represents the results for $T_{eff}=36300 \text{ K}$ and $Q(H)_2=10^{50.5} \text{ s}^{-1}$. The grey long-dashed line with circles has additional $Q(H)_1=10^{49.0} \text{ s}^{-1}$.

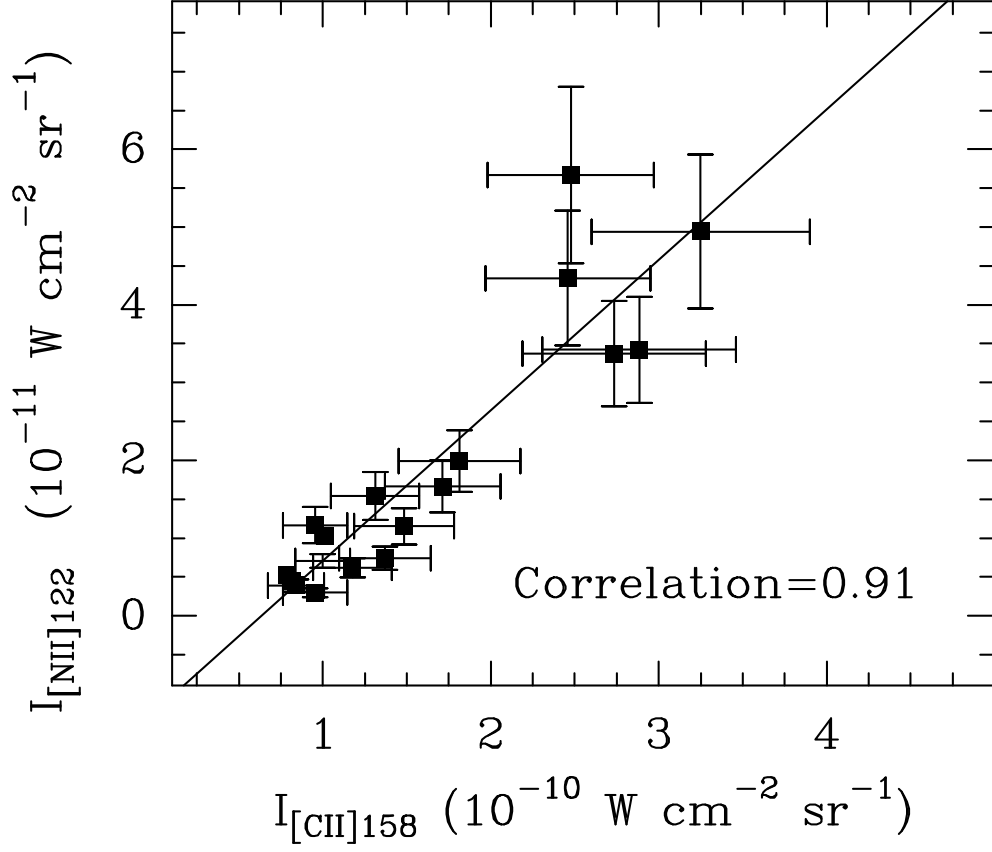


Fig. 5.— Correlation between the [N II]122 μm and [C II]158 μm lines. Each source position have been corrected for its minimum visual extinction derived from far-IR continuum fits (see table 3). Sgr B2(M,N) positions are not included (see text).

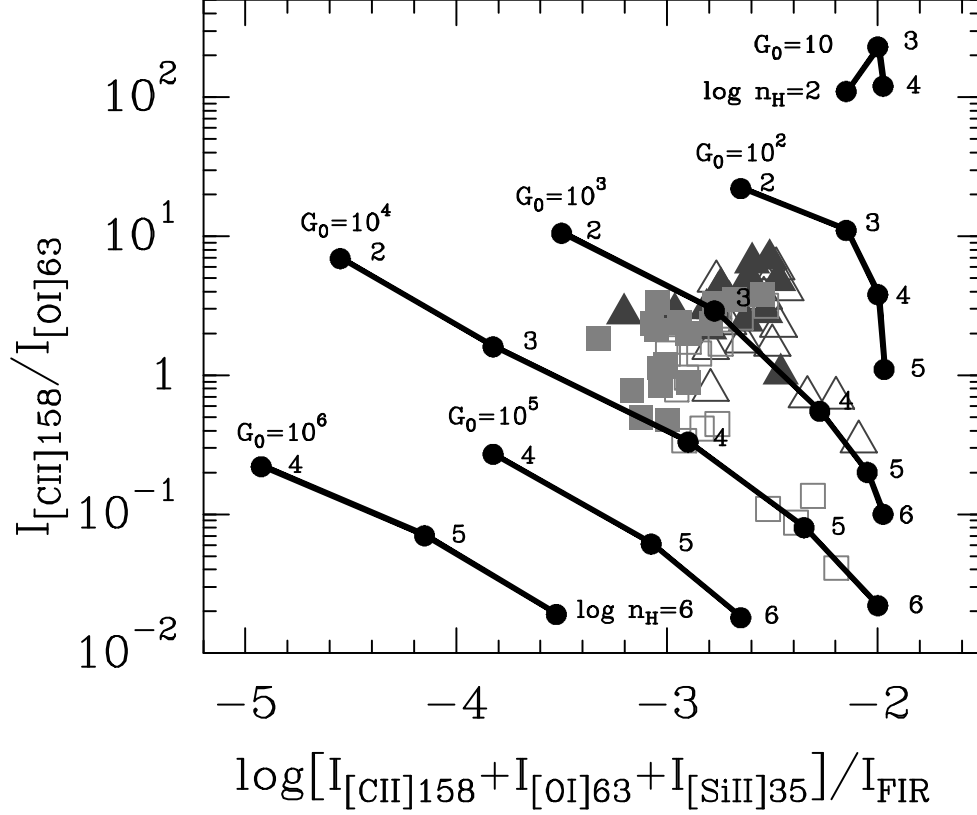


Fig. 6.— $[C\text{ II}]/[O\text{ I}]$ intensity ratio vs. $([C\text{ II}]+[O\text{ I}]+[Si\text{ II}])/far\text{-IR}$ for several PDR models of varying far-UV fields and hydrogen densities (from WHT90). The different points of Sgr B2 are shown in gray. Dark gray triangles for calculations that consider all the observed $[C\text{ II}]$ intensity at each position and light gray squares for a mean $[C\text{ II}]$ intensity from PDRs of $6.4 \times 10^{-11} \text{ W cm}^{-2} \text{ sr}^{-1}$ in all positions. The different points represent the intensity ratios corrected for the minimum (filled) and maximum (not filled) visual extinction (see Table 3).

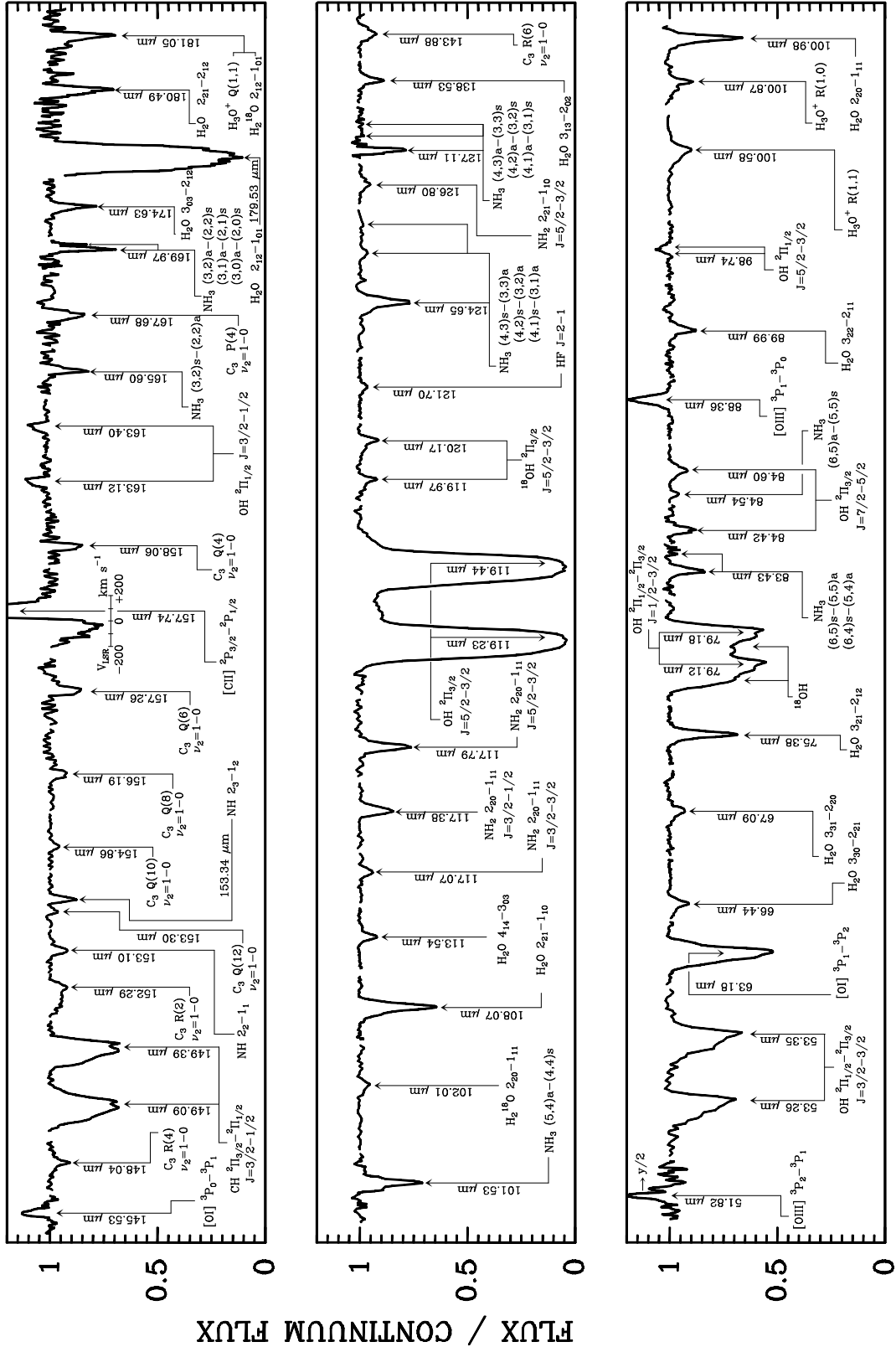


Fig. 7.— Far-IR features in the spectrum of Sgr B2(M) taken with the ISO/LWS Fabry-Perot with a spectral resolution of $\sim 35 \text{ km s}^{-1}$. Note the wavelength discontinuity of the spectrum after each line. Some weak features remain unidentified (not shown) while some detections have been discussed in other works (see tables 4 and 5 and text references).

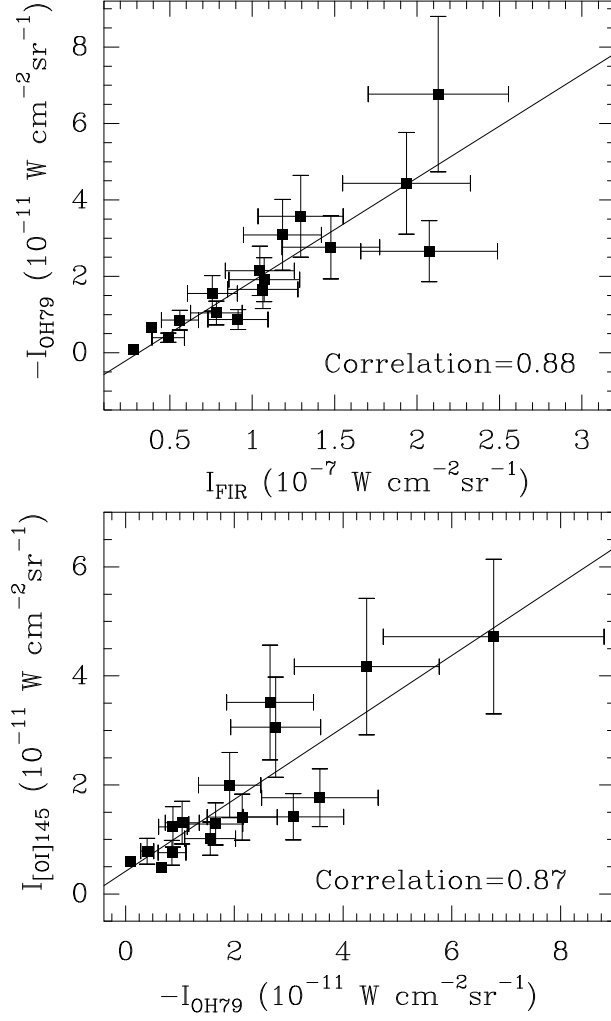


Fig. 8.— *Top*: Observed correlation between the OH $\sim 79 \mu\text{m}$ absorption and the far-IR continuum emission. *Bottom*: Observed correlation between the [OI] $145 \mu\text{m}$ emission and the OH $\sim 79 \mu\text{m}$ absorption. Both figures exclude the (M,N) and $\Delta\delta = -90''$ obscured positions.

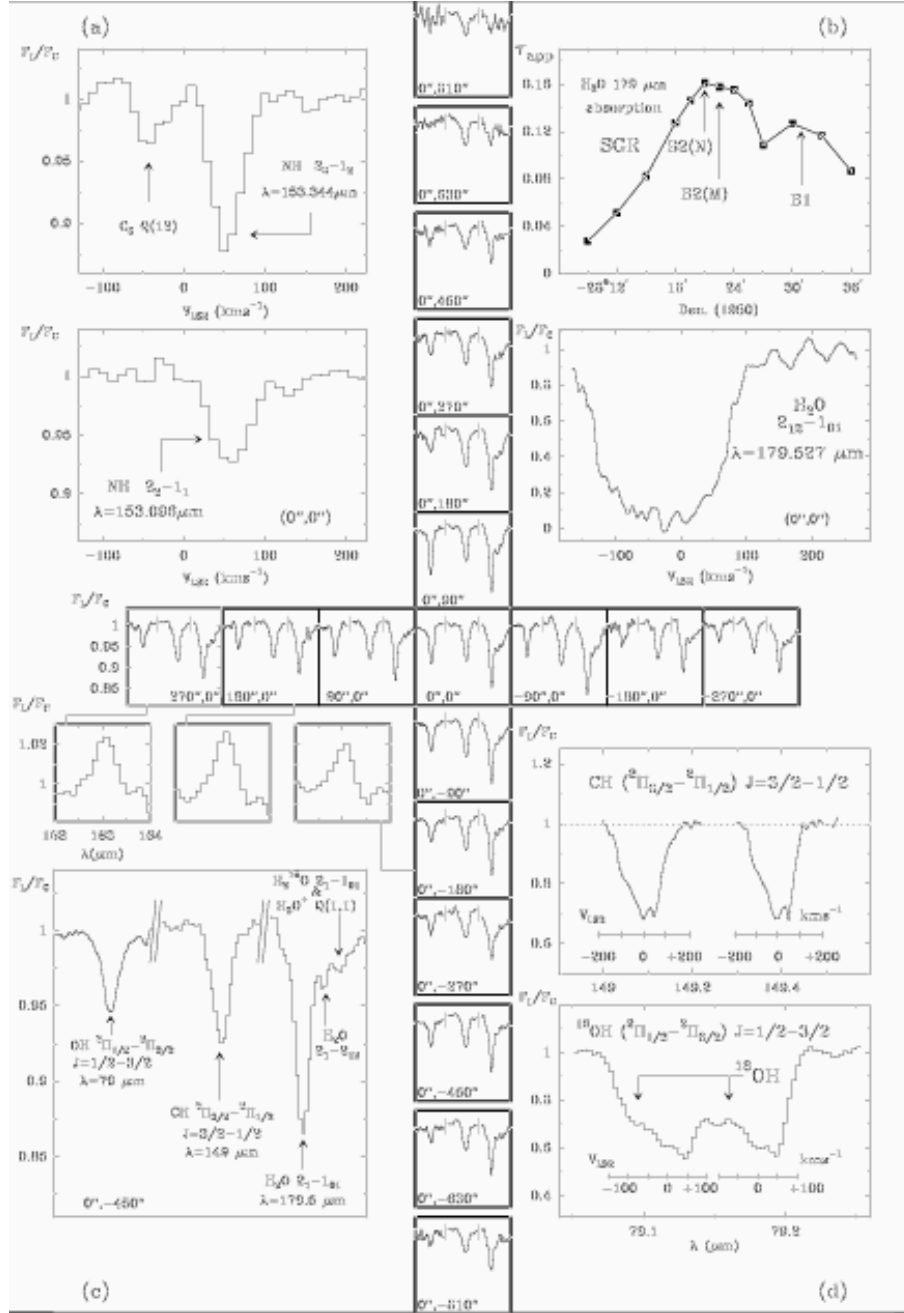


Fig. 9.— Raster map obtained with the LWS grating of the OH($\sim 79 \mu\text{m}$), CH($\sim 149 \mu\text{m}$) and H_2O ($\sim 179 \mu\text{m}$) lines. Detections of an emission feature at $\sim 163 \mu\text{m}$ are also presented. In each box, offset positions are given in arcsec respect to the $(0'', 0'')$ central position at: $\alpha = 17^{\text{h}}44^{\text{m}}10.61^{\text{s}}$, $\delta = -28^{\circ}22'30.0''$ [J1950]. The intensity scale corresponds to the continuum normalized flux and the abscissa to the wavelength. (a) NH lines detected with the LWS-FP in $(0'', 0'')$ around $\sim 153 \mu\text{m}$. (b) *Top*: $\text{H}_2\text{O } 2_{12}-1_{01}$ apparent opacity in the north-to-south declination raster with main sources position labelled. *Bottom*: Fundamental o- H_2^{16}O line detected with the LWS-FP in $(0'', 0'')$ around $\sim 179 \mu\text{m}$. (c) Main features of the grating raster map labelled. (d) CH and OH Λ -doublets detected with the LWS-FP in $(0'', 0'')$ around ~ 149 and $\sim 79 \mu\text{m}$, respectively.

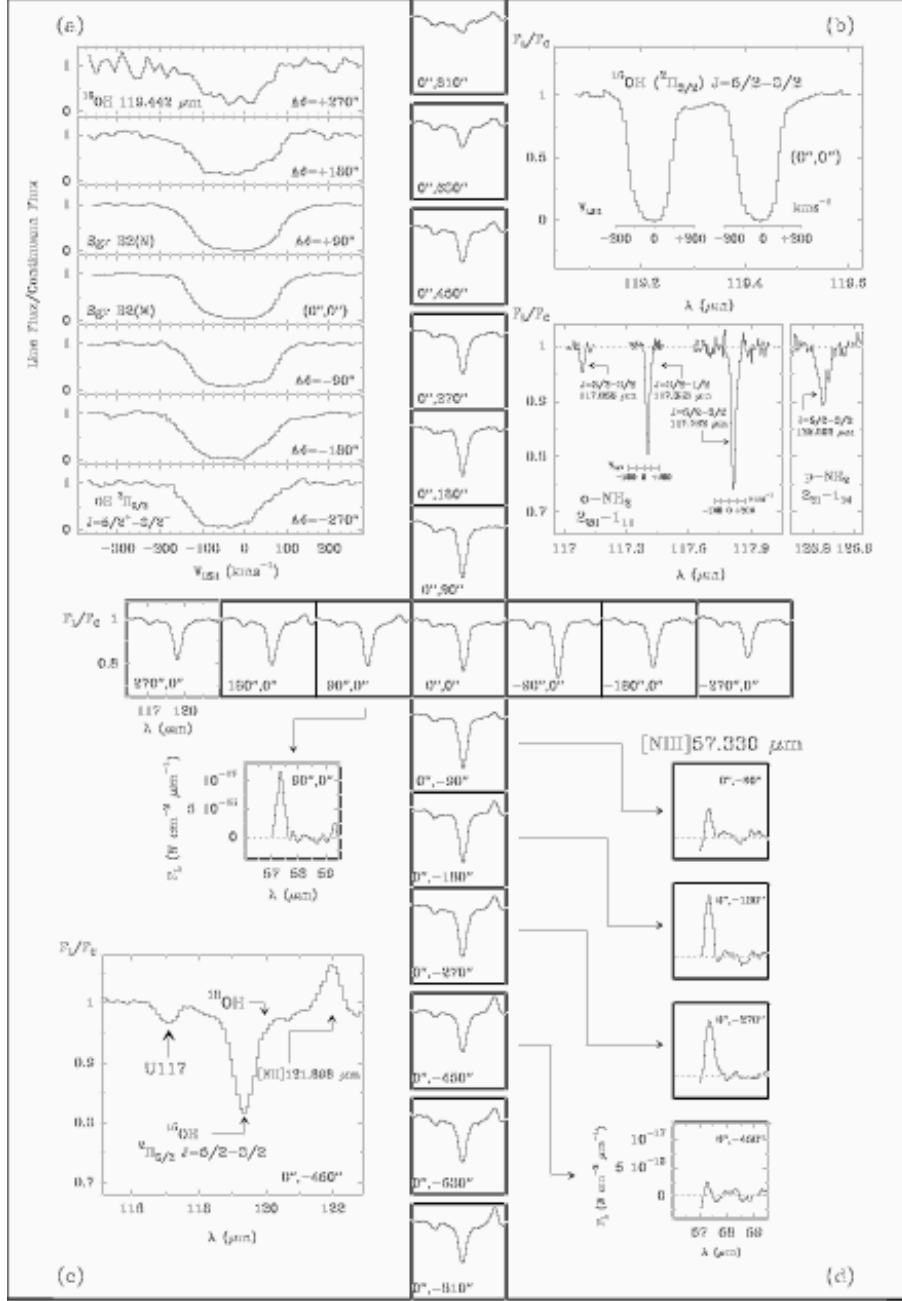


Fig. 10.— Raster map obtained with the LWS grating between 115–121 μm . In each box, offset positions are given in arcsec respect to the $(0'', 0'')$ central position at: $\alpha = 17^{\text{h}}44^{\text{m}}10.61^{\text{s}}$, $\delta = -28^{\circ}22'30.0''$ [J1950]. The intensity scale corresponds to the continuum normalized flux and the abscissa to the wavelength. (a) LWS-FP declination raster of the ^{16}OH 119.442 μm line. (b) *Top*: Fundamental OH A-doublet detected with the LWS-FP in $(0'', 0'')$ around $\sim 119 \mu\text{m}$. *Bottom*: ortho and para NH_2 lines detected with the LWS-FP in $(0'', 0'')$ around ~ 117 and $126 \mu\text{m}$. The NH_2 ~ 117 triplet may contribute to the U117 line observed at much lower resolution. (c) Main features of the grating raster map labelled. (d) Raster map positions with clear $[\text{N III}] 57 \mu\text{m}$ detections.

Table 1. Fluxes derived from gaussian fits to the fine structure lines observed with the LWS grating. Fluxes are in units of 10^{-19} W cm $^{-2}$ and numbers in parentheses are the statistical errors. Offsets (in arcsec) respect to the map center, Sgr B2(M).

$\lambda(\mu\text{m})$ map position	[C II] 157.741	[O I] 145.525	[N II] 121.898	[O III] 88.356	[O I] 63.184	[N III] 57.317	[O III] 51.815
(0,810)	68.0(2.3)	5.1(0.1)	5.6(0.5)	2.8(1.2)	20.1(1.2)	<4	<7
(0,630)	69.4(2.5)	4.1(0.4)	4.8(1.1)	4.0(1.5)	21.3(1)	<3	7.8(4.1)
(0,450)	86.0(4.1)	6.4(0.6)	10.9(1.7)	5.9(0.2)	31.2(1.5)	<1	8.6(2.2)
(0,270)	79.0(5.8)	8.4(3.3)	3.0(1.0)	4.1(0.9)	33.0(1.2)	<4	<5
(0,180)	62.6(5.9)	10.3(6.0)	3.4(0.5)	4.3(1.0)	20.6(1.5)	<4	<6
(0,90)	— ^a	42.0(1.3)	<35	28.4(4.2)	-14.9(2.9)	<11	8.2(3.1)
(0,0)	— ^a	73.3(8.2)	<44	41.5(17.2)	-137.2(18.1)	<17	21.9(6.2)
(0,-90)	149.0(10.5)	39.9(1.0)	18.5(4.6)	71.5(8.3)	25.6(2.6)	8.1(2.4)	26.3(4.7)
(0,-180)	237.2(8.8)	29.7(3.3)	41.6(6.0)	98.0(4.7)	83.7(3.6)	21.7(2.9)	60.0(7.1)
(0,-270)	235.3(6.7)	24.7(2.1)	33.9(3.6)	67.4(6.7)	73.2(2.7)	25.5(2.9)	25.9(3.4)
(0,-450)	210.7(4.0)	14.9(1.4)	39.6(4.6)	19.9(3.2)	63.6(1.4)	11.1(3.5)	22.8(7.9)
(0,-630)	146.6(4.5)	11.1(0.5)	17.6(3.6)	10.5(1.5)	31.0(3.8)	5.3(3.6)	20.6(10.6)
(0,-810)	113.8(2.0)	6.8(0.5)	16.6(1.0)	15.0(1.4)	23.3(1.7)	3.3(1.2)	9.2(1.1)
(270,0)	104.3(6.0)	13.6(1.7)	9.1(1.6)	6.3(1.5)	38.9(2.6)	<4	<1
(180,0)	144.7(5.6)	11.1(1.1)	19.0(2.0)	18.1(1.6)	46.9(2.6)	<7	18.1(2.9)
(90,0)	174.2(7.8)	32.5(2.1)	35.0(2.8)	67.9(4.5)	45.9(2.0)	28.1(3.0)	26.1(4.0)
(-90,0)	60.6(8.7)	21.4(2.4)	<8	13.4(3.4)	12.6(1.9)	<3	5.1(8.5)
(-180,0)	108.0(4.9)	10.0(1.1)	<7	11.0(7.0)	23.3(1.8)	<3	3.9(1.9)
(-270,0)	94.8(5.0)	9.8(0.6)	<6	9.7(1.3)	17.8(1.3)	<4	3.4(0.3)

^aAt the low resolution of the LWS/grating, the [C II]158 μm line is not detected in Sgr B2(M,N). When observed at higher resolution (see Fig. 3b) the resolved line profile shows an absorption feature produced by the foreground gas that reduce the expected line flux in the grating to the noise level of the spectra. Hence, the non detection in the grating is consistent with the detection in the FP.

Table 2. Dust temperatures derived by fitting the far-IR continuum emission with 2 gray bodies and luminosities in the LWS range.

position ^a	T_{dust}^{warm} (K)	T_{dust}^{cold} (K)	$L_{LWS}(L_{\odot})$
(0,810)	30-33	17-20	6.91E4
(0,630)	30-33	17-20	9.57E4
(0,450)	31-35	18-22	1.37E5
(0,270)	25-29	13-20	1.86E5
(0,180)	26-35	16-20	2.56E5
(0,-90)	27-30	17-19	6.20E5
(0,-180)	32-36	18-21	4.74E5
(0,-270)	34-38	18-22	3.61E5
(0,-450)	36-38	17-20	3.17E5
(0,-630)	32-34	18-21	1.91E5
(0,-810)	34-37	18-22	1.20E5
(270,0)	25-27	14-19	2.63E5
(180,0)	29-32	17-20	2.90E5
(90,0)	31-34	18-20	5.21E5
(-90,0)	24-26	15-19	5.07E5
(-180,0)	24-26	13-19	2.60E5
(-270,0)	24-25	13-19	2.24E5

^aOffsets (in arcsec) respect to Sgr B2(M).

Table 3. Selected line ratios after correcting for the two limits of visual extinction (A_V^{min} and A_V^{max}) derived for best-fit gray body models ($\beta=1.0-1.5$). The different beam sizes of each LWS detector are taken into account and extended emission is considered.

map position ^a	warm dust A_V (mag)	cold dust A_V (mag)	[O III] R(52/88)	n_e ([O III]) $\log(\text{cm}^{-3})$	[N III]/[N II] R(57/122)	T_{eff} ($\div 10^3$ K)
(0,810)	1.2-1.5	15-55	<2.40	<3.18	<0.72	<33.2
(0,630)	1.6-2.0	23-84	1.79-2.23	2.83-3.10	<0.72	<33.2
(0,450)	1.1-1.8	25-92	1.36-1.73	2.49-2.79	<0.26	<31.8
(0,270)	5.2-8.0	41-112	<1.61	<2.70	<1.77	<35.6
(0,180)	0.7-1.7	131-294	<3.55	<3.66	<2.73	<35.2
(0,-90)	16-18	367-877	1.27-8.11	2.41-4.67	1.60-11.3	(35.0-37.2)
(0,-180)	3.7-5.2	148-493	0.90-3.18	1.99-3.53	0.78-2.95	(34.9-35.3)
(0,-270)	2.8-3.8	59-205	0.41-0.69	1.03-1.67	0.79-1.39	(35.0-35.8)
(0,-450)	3.2-5.3	91-249	1.47-2.64	2.59-3.30	0.35-0.64	(32.2-33.1)
(0,-630)	3.5-3.9	23-85	1.83-2.30	2.85-3.13	0.28-0.36	(31.9-32.2)
(0,-810)	1.1-1.3	16-59	0.55-0.64	1.39-1.58	0.18-0.21	(32.8-33.1)
(270,0)	27-28	156-536	<1.19	<2.24	<3.13	<36.6
(180,0)	4.9-6.6	78-276	1.14-2.38	2.28-3.18	<0.95	<33.6
(90,0)	7.4-9.0	168-565	0.62-2.64	1.53-3.30	1.31-6.07	(35.7-36.3)
(-90,0)	28-34	228-579	0.85-2.97	1.92-3.44	—	—
(-180,0)	21-26	62-168	0.43-0.63	1.10-1.55	—	—
(-270,0)	21-25	45-124	0.38-0.50	0.94-1.27	—	—

^aOffsets (in arcsec) respect to the map center, Sgr B2(M).

Table 4. Published Far-IR features detected with the LWS/FP toward Sgr B2(M) between 181.1-119.6 μm

species	transition	$\lambda_{rest}(\mu\text{m})$	references
H ₃ O ⁺	$1_1^- - 1_1^+$	181.05	(5)
H ₂ ¹⁸ O	$2_{12} - 1_{01}$	181.05	(2),(5),(11)
H ₂ O	$2_{21} - 2_{12}$	180.49	(11)
H ₂ O	$2_{12} - 1_{01}$	179.53	(2),(11)
H ₂ O	$3_{03} - 2_{12}$	174.63	(2),(11)
NH ₃	$(3, 2)a - (2, 2)s$	169.97	(7)
C ₃	$P(4) \nu_2 = 1 - 0$	167.68	(4)
NH ₃	$(3, 2)s - (2, 2)a$	165.60	(7)
OH	$^2\Pi_{1/2} J = 3/2^- - 1/2^+$	163.40	(8)
OH	$^2\Pi_{1/2} J = 3/2^+ - 1/2^-$	163.12	(8)
C ₃	$Q(4) \nu_2 = 1 - 0$	158.06	(4)
C ⁺	$^2P_{3/2} - ^2P_{1/2}$	157.74	(1),(10)
C ₃	$Q(6) \nu_2 = 1 - 0$	157.26	(4)
H ₂ O	$3_{22} - 3_{13}$	156.19	(11)
C ₃	$Q(8) \nu_2 = 1 - 0$	156.19	(4)
C ₃	$Q(10) \nu_2 = 1 - 0$	154.86	(4)
NH	$2_3 - 1_2$	153.34	(4)
C ₃	$Q(12) \nu_2 = 1 - 0$	153.30	(4)
NH	$2_2 - 1_1$	153.10	(1)
C ₃	$R(2) \nu_2 = 1 - 0$	152.29	(4),(16)
CH	$^2\Pi_{3/2} - ^2\Pi_{1/2} J = 3/2^- - 1/2^+$	149.39	(1),(13)
CH	$^2\Pi_{3/2} - ^2\Pi_{1/2} J = 3/2^+ - 1/2^-$	149.09	(1),(13)
C ₃	$R(4) \nu_2 = 1 - 0$	148.04	(4)
O ⁰	$^3P_0 - ^3P_1$	145.53	(1),(10)
C ₃	$R(6) \nu_2 = 1 - 0$	143.88	(4)
H ₂ O	$3_{13} - 2_{02}$	138.53	(11)
NH ₃	$(4, 3)a - (3, 3)s$	127.11	(7)
NH ₂	$2_{21} - 1_{10} J = 5/2 - 3/2$	126.80	(1)
NH ₃	$(4, 2)s - (3, 2)a$	124.80	(7)
NH ₃	$(4, 3)s - (3, 3)a$	124.65	(7)
HF	$J = 2 - 1$	121.70	(3)
¹⁸ OH	$^2\Pi_{3/2} J = 5/2^+ - 3/2^-$	120.17	(8),(14)
¹⁸ OH	$^2\Pi_{3/2} J = 5/2^- - 3/2^+$	119.97	(8),(14)
¹⁷ OH	$^2\Pi_{3/2} J = 5/2^+ - 3/2^-$	119.83	(12)
¹⁷ OH	$^2\Pi_{3/2} J = 5/2^- - 3/2^+$	119.62	(12)

Table 5. Published Far-IR features detected with the LWS/FP toward Sgr B2(M) between 119.4-51.8 μm

species	transition	$\lambda_{rest}(\mu\text{m})$	references
OH	${}^2\Pi_{3/2} \ J = 5/2^+ - 3/2^-$	119.44	(2),(8),(15)
OH	${}^2\Pi_{3/2} \ J = 5/2^- - 3/2^+$	119.23	(8),(15)
NH ₂	$2_{20} - 1_{11} \ J = 5/2 - 3/2$	117.79	(1)
NH ₂	$2_{20} - 1_{11} \ J = 3/2 - 1/2$	117.38	(1)
NH ₂	$2_{20} - 1_{11} \ J = 3/2 - 3/2$	117.07	(1)
H ₂ O	$4_{14} - 3_{03}$	113.54	(11)
HD	$J = 1 - 0$	112.07	(9)
H ₂ O	$2_{21} - 1_{10}$	108.07	(11)
H ₂ ¹⁸ O	$2_{20} - 1_{11}$	102.01	(11)
NH ₃	$(5, 4)a - (4, 4)s$	101.53	(7)
H ₂ O	$2_{20} - 1_{11}$	100.98	(5), (11)
H ₃ O ⁺	$2_0^- - 1_0^+$	100.87	(5)
H ₃ O ⁺	$2_1^- - 1_1^+$	100.58	(5)
NH ₃	$(5, 3)s - (4, 3)a$	100.11	(7)
NH ₃	$(5, 4)s - (4, 4)a$	99.95	(7)
OH	${}^2\Pi_{1/2} \ 5/2 - 3/2$	98.74	(8)
H ₂ O	$3_{22} - 2_{11}$	89.99	(11)
O ⁺⁺	${}^3P_1 - {}^3P_0$	88.36	(1)
OH	${}^2\Pi_{3/2} \ J = 7/2^- - 5/2^+$	84.60	(2),(8)
NH ₃	$(6, 5)a - (5, 5)s$	84.54	(7),(8)
OH	${}^2\Pi_{3/2} \ J = 7/2^+ - 5/2^-$	84.42	(8)
NH ₃	$(6, 5)s - (5, 5)a$	83.43	(7)
OH	${}^2\Pi_{1/2} - {}^2\Pi_{3/2} \ J = 1/2^+ - 3/2^-$	79.18	(8)
OH	${}^2\Pi_{1/2} - {}^2\Pi_{3/2} \ J = 1/2^- - 3/2^+$	79.12	(8)
H ₂ O	$3_{21} - 2_{12}$	75.38	(11)
NH ₃	$(7, 6)a - (6, 6)s$	72.44	(7)
NH ₃	$(7, 6)s - (6, 6)a$	71.61	(7)
H ₂ O	$3_{31} - 2_{20}$	67.09	(11)
H ₂ O	$3_{30} - 2_{21}$	66.44	(11)
NH ₃	$(8, 7)a - (7, 7)s$	63.38	(7)
O ⁰	${}^3P_1 - {}^3P_2$	63.18	(6),(10)
NH ₃	$(8, 7)s - (7, 7)a$	62.73	(7)
NH ₃	$(9, 8)a - (8, 8)s$	56.34	(7)
OH	${}^2\Pi_{1/2} - {}^2\Pi_{3/2} \ J = 3/2^- - 3/2^+$	53.35	(8)
OH	${}^2\Pi_{1/2} - {}^2\Pi_{3/2} \ J = 3/2^+ - 3/2^-$	53.26	(8)
O ⁺⁺	${}^3P_2 - {}^3P_1$	51.82	(1)

References. — (1) This paper; (2) Cernicharo et al. 1997; (3) Neufeld et al. 1997; (4) Cernicharo et al. 2000; (5) Goicoechea & Cernicharo 2001; (6) Lis et al. 2001; (7) Ceccarelli et al. 2002; (8) Goicoechea & Cernicharo 2002; (9) Polehampton et al. 2002; (10) Vastel et al. 2002; (11) Cernicharo et al., 2004 in prep.; (12) Polehampton et al., 2003 in prep.; (13) Stacey et al. 1987 (with KAO); (14) Lugten et al. 1986 (with KAO); (15) Storey et al. 1981 (with KAO); (16) Giesen et al. 2001 (with KAO).